SACLANTCEN Report
SR – 71

SACLANT ASW RESEARCH CENTRE REPORT

EXPLOSION-GENERATED SEISMIC INTERFACE WAVES IN SHALLOW WATER : EXPERIMENTAL RESULTS

by

Bernd SCHMALFELDT and Dieter RAUCH

1 JULY 1983

NORTH
ATLANTIC
TREATY
ORGANIZATION

LA SPEZIA, ITALY

Published by

STI

SACLANTCEN REPORT SR-71

NORTH ATLANTIC TREATY ORGANIZATION

SACLANT ASW Research Centre
Viale San Bartolomeo 400, I-19026 San Bartolomeo (SP), Italy.

tel: national 0187 560940
international + 39 187 560940
telex: 271148 SACENT I

EXPLOSION-GENERATED SEISMIC INTERFACE WAVES IN SHALLOW WATER: EXPERIMENTAL RESULTS

by

Bernd Schmalfeldt and Dieter Rauch

1 July 1983

This report has been prepared as part of Project 05.

APPROVED FOR DISTRIBUTION

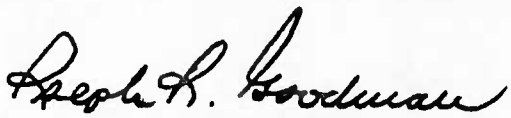

RALPH R. GOODMAN
Director

TABLE OF CONTENTS

	Pages
ABSTRACT	1
INTRODUCTION	3
1 PHYSICAL BACKGROUND	5
2 TECHNICAL BACKGROUND	7
2.1 The SACLANTCEN Ocean-Bottom Seismometer and associated equipment	7
2.2 Experimental procedure	10
3 PRESENTATION OF RESULTS	13
3.1 Time/distance plots	13
3.2 Group-velocity dispersion analysis curves (amplitude contours)	14
3.3 Attenuation curves	14
4 EXPERIMENTAL RESULTS	17
4.1 Experiment P	17
4.2 Experiment M	26
4.3 Experiment G	29
4.4 Experiment R	41
CONCLUSIONS	53
ACKNOWLEDGMENTS	55
REFERENCES	57
APPENDIX A - ACQUISITION AND PRE-PROCESSING OF SEISMIC DATA	61
APPENDIX B - DISPERSION ANALYSIS WITH THE "MULTIPLE-FILTER TECHNIQUE"	63
APPENDIX C - ATTENUATION ANALYSIS BY MEANS OF THE "SPECA" SYSTEM	67

List of Figures

1.	Location of the measurement sites.	2
2.	Seismograms and resulting hodographs.	5
3.	The ocean-bottom seismometer (OBS).	7
4.	Electronic block diagram.	9
5.	Deployment of OBS system and experimental procedure.	11
6.	Methods of presenting experimental results.	15
7.	Site P, Run 2: Time/distance plots.	18
8.	Site P, Run 2: Amplitude contours from event "→" of Fig. 7.	19
9.	Site P, Run 2: Seismograms and resulting hodographs.	21
10.	Site P, Run 2: Attenuation curves.	22
11.	Site P, Run 3: Time/distance plots.	23

	Pages
12. Site P, Run 3: Amplitude contours from event "→" of Fig. 11.	24
13. Site P, Run 3: Attenuation curves.	25
14. Site M, Run 5: Time/distance plots.	27
15. Site M, Run 5: Amplitude contours.	27
16. Site M, Run 6: Time/distance plots.	28
17. Site G, Run 7(A): Time/distance plots from close OBS.	30
18. Site G, Run 7(A): Time/distance plots from distant OBS.	31
19. Site G, Run 7(A): Amplitude contours from event "→" of Fig. 17.	34
20. Site G, Run 7(A): Amplitude contours from event "→" of Fig. 18.	35
21. Site G, Run 7(B): Time/distance plots (close OBS).	36
22. Site G, Run 7(B): Time/distance plots (distant OBS).	37
23. Site G, Run 7(B): Amplitude contours from event "→" of Fig. 21.	38
24. Site G, Run 7(B): Amplitude contours from event "→" of Fig. 22.	39
25. Site G, Run 8: Attenuation curves from Run 7 (A & B).	40
26. Site R, Run 8: Time/distance plots (first OBS).	44
27. Site R, Run 8: Time/distance plots (second OBS).	45
28. Site R, Run 8: Time/distance plots (third OBS).	46
29. Site R, Run 8: Amplitude contours from event "→" of Fig. 26 (first OBS).	47
30. Site R, Run 8: Attenuation curves.	48
31. Site R, Run 9: Time/distance plots (first OBS).	49
32. Site R, Run 9: Time/distance plots (second OBS).	50
33. Site R, Run 9: Amplitude contours from event "→" of Fig. 31 (first OBS).	51
34. Site R, Run 9: Attenuation curves.	52

EXPLOSION-GENERATED SEISMIC INTERFACE WAVES IN SHALLOW WATER: EXPERIMENTAL RESULTS

by

Bernd Schmalfeldt and Dieter Rauch

ABSTRACT

Seismic interface waves of the Stoneley/Scholte type propagate along the ocean bottom and enable sound to be transmitted at frequencies below the acoustic cut-off frequency of shallow-water ducts. The results of four major sea-trials close to La Spezia, Italy, in the period 1979-81 are presented. The experiments provided a good understanding of the propagation of infrasound in shallow waters, together with some results of the attenuation and excitation of these waves. An attempt was made to explore the use of interface waves for obtaining the values of some of the physical parameters of sea-floor sediments that affect the transmission of these waves.

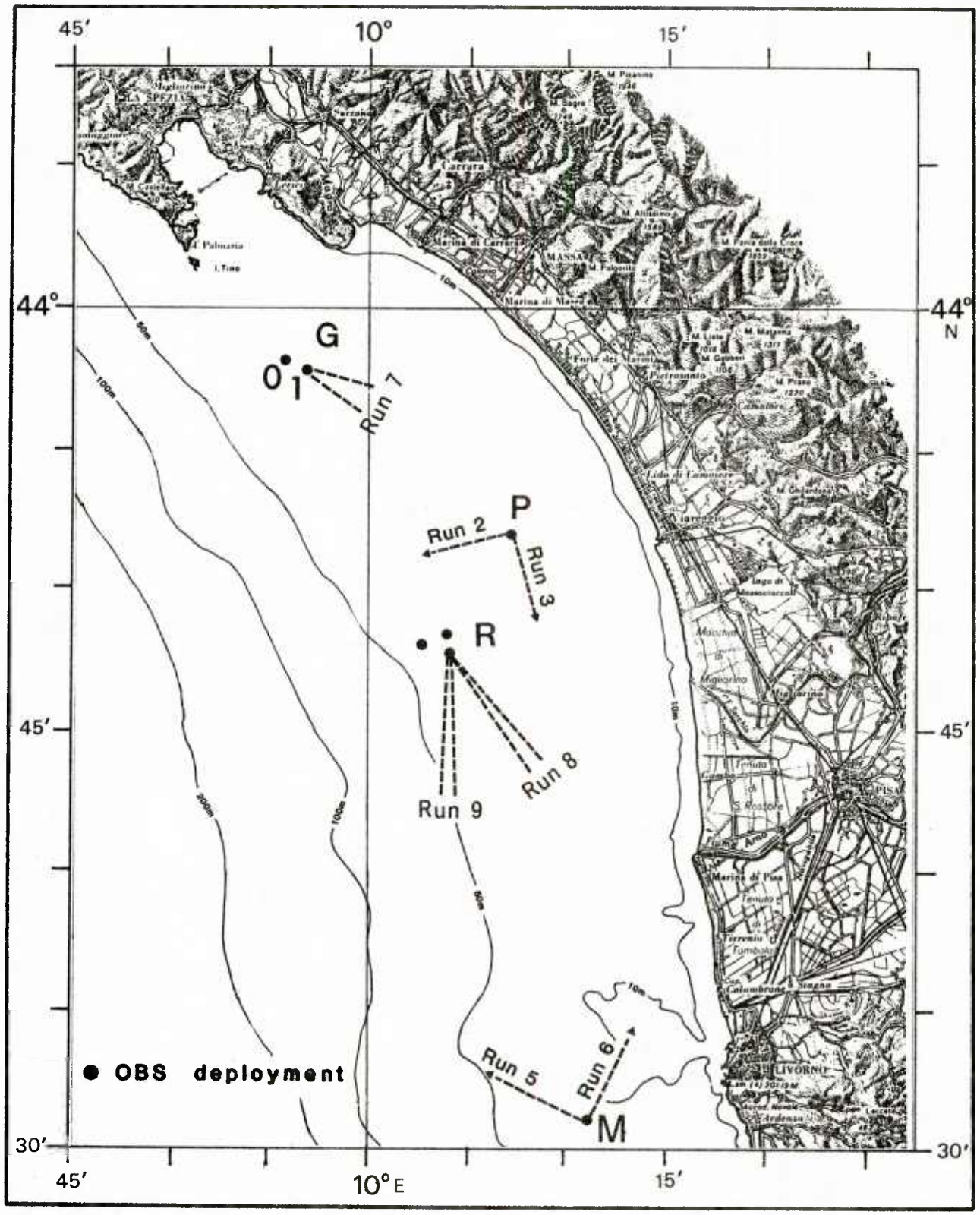

FIG. 1 LOCATIONS OF THE MEASUREMENT SITES

INTRODUCTION

Theoretical studies and many acoustic measurements in shallow waters have demonstrated that infrasound transmission in the water column is highly attenuated below the acoustic cut-off frequency. In a liquid layer on top of a solid half-space, the only propagation mode that does not suffer such a cut-off is the seismic interface wave. This wave type is nothing else than the lowest mode of the water/solid half-space system. This Stoneley, or Scholte-type wave is trapped by the acoustically most significant interface separating the liquid overburden (including unconsolidated, liquid-like sediments) from the solid underground <1 to 3>. This mode is usually split into different branches (dispersion) by the layering of the bottom or the depth-dependence of the bottom parameters.

Theoretical microseismic studies <4> in which the water layer has been treated as a kind of perturbation for long-period Rayleigh waves have demonstrated that the ratio of the bottom pressure in the water column to the vertical particle velocity of the sea-floor surface is a sensitive indicator of the shear characteristics of the bottom structure <5>. Subsequent measurements of the microseismic noise with ocean-bottom seismometers <6> have extended these conclusions to short-period waves, i.e. to the interface waves of the Stoneley/Scholte type.

Recent theoretical studies by Hawker <7,8> have shown that well-known sea-floor reflection anomalies can be explained by the generation of these interface waves.

In principle, these seismic waves can be detected by bottom-mounted hydrophones, but only the use of triaxial seismometers allows all the information offered by the vectorial character of these waves to be exploited. In late 1978 SACLANTCEN therefore developed its Ocean-Bottom Seismometers (OBS), equipped with three orthogonal geophones and one hydrophone, for use in these studies.

During the 1979-81 period OBS were operated in shallow waters — sometimes singly, sometimes in pairs, and sometimes in groups of three — to study the propagation of interface waves generated by explosions, ship propellers, and LF-projectors, and to record low-frequency ambient noise.

The locations of the four major sea-trials, which took place off the Versilian coast of the upper Tyrrhenian Sea, are illustrated in Fig. 1. This report presents only the results of those field experiments that dealt with the propagation of explosion-generated interface waves.

1 PHYSICAL BACKGROUND

Seismic interface waves are those waves that are guided by the water/bottom interface or, more strictly speaking, by the acoustically most significant sediment interface separating the water column from the more consolidated sea-floor. In seismic studies they are usually described as Stoneley waves, but, following a suggestion of Caignard <2>, the designation Scholte wave is used to emphasize the presence of a liquid overburden.

The following summarizes the most significant characteristics of seismic interface waves. In the case of laterally homogeneous sediment layers the particle motion of these waves is always confined to the plane that includes the source/receiver direction and the vertical on the interface (i.e. to the radial/vertical plane). Between the radial and vertical ground displacements there is a rather stable phase shift of about $\pm \pi/2$ and a high coherence. This results in quite regular elliptical particle orbits or hodographs, as previous studies have shown <9,10>. These elliptical motions are illustrated indicatively, together with the associated seismograms, in Fig. 2. A negative phase shift (counterclockwise elliptical orbits) is referred to as a retrograde particle motion, a positive phase shift (clockwise elliptical orbits, as in the example of Fig. 2) as prograde particle motion. This strongly polarized geometrical pattern (ellipse) permits both the identification of the wave type and the determination of the direction to the source, with an ambiguity of 180°. However, this 180° ambiguity can be overcome by exploiting also the "sense" of the elliptical motion, as demonstrated in <11>.

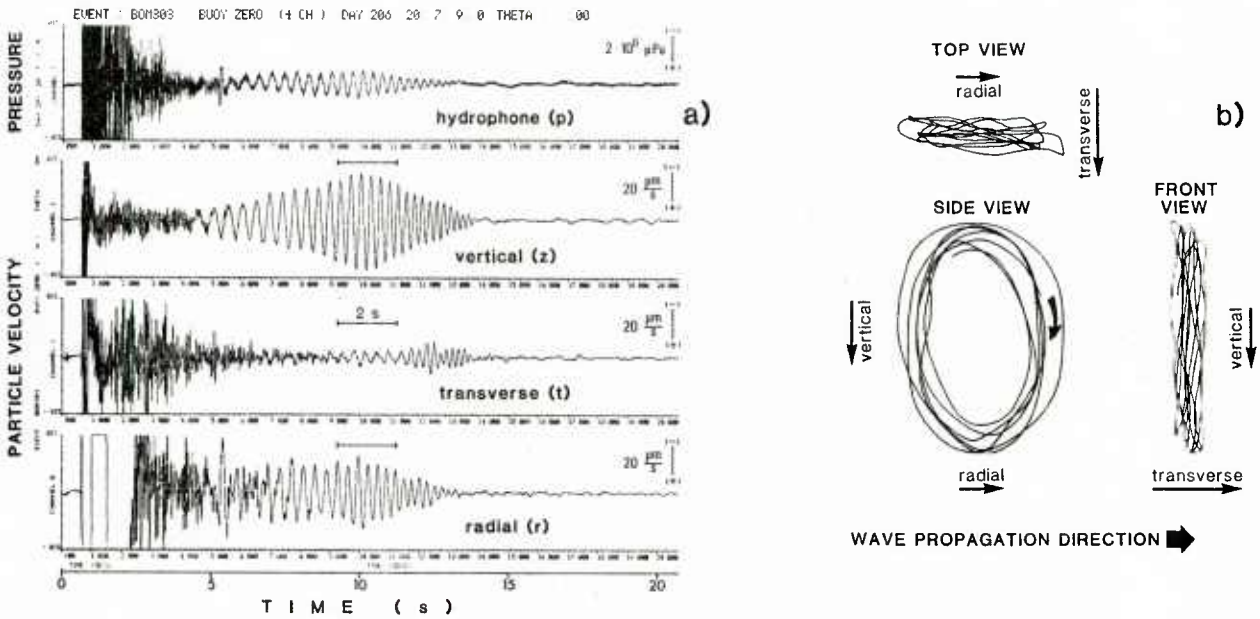

FIG. 2 SEISMOGRAMS AND RESULTING HODOGRAPHS
a. Seismograms from the three geophones and the hydrophone of an ocean-bottom seismometer
b. Resulting hodograph in three planes

Similar phase and coherence relations exist between the bottom pressure in the water column and the vertical particle velocity at the bottom, as reported for instance in <6>.

The energy carried in these waves decreases exponentially perpendicular to the interface, the "penetration depth" being characterized roughly by one wavelength. Therefore these waves are less subject to radiation losses than other basic wave types (bulk waves). Consequently, these waves are most easily sensed, or monitored, in the region of the immediate interface. Similarly, the excitation of this wave type is better the closer the source is located to the interface, as demonstrated in <10>.

The associated phase velocities are always less than the sound speed in water, c_w, (at the bottom of the water column) and the shear-velocity in the sea-floor, c_s. At the surface of unconsolidated sediments the ratio c_s/c_p of the shear velocity to the compressional velocity is usually of the order of 0.2 to 0.35 <12>, and the compressional velocity (c_p) is of the order of the sound speed in water (c_w). Hence phase velocities of around some 100 to 250 m/s are to be expected for Scholte waves.

2 TECHNICAL BACKGROUND

2.1 The SACLANTCEN Ocean-Bottom Seismometer and Associated Equipment

2.1.1 The Ocean-Bottom Seismometer (Figs. 3 and 4a)

An ocean-bottom seismometer (OBS) was designed and developed at SACLANTCEN <13> on the basis of a previous design that had resulted from earlier studies <14>.

This OBS unit (Fig. 3) comprises sensors, preamplifiers, and analogue/digital electronics. It is powered, via a thin coaxial cable, by a battery in a surface buoy (see Sect. 2.1.2). The geoacoustic and auxiliary sensors consist of:

- Three relatively light and small active 1-Hz geophones (Teledyne S-500) that can be operated in any orientation and do not need locking for transportation and handling.
- An omnidirectional hydrophone mounted outside the OBS or floating above it.
- Two tilt-meters to monitor the inclination of the OBS to the seafloor.
- A compass to determine the OBS orientation.
- A thermistor.

FIG. 3 THE OCEAN-BOTTOM SEISMOMETER (OBS)

Figure 4a shows the electronics. The analogue signals generated by the sensors are amplified, filtered and digitized by two A/D converters operating at different sampling rates. One, devoted to the auxiliary sensors and check points, operates at low speed at 25 Hz/channel. The other samples the four geoacoustic sensors (three geophones and a hydrophone) at 600 Hz/channel, allowing a nominal bandwidth of 200 Hz/channel. The two outputs, together with parity controls and synchronization patterns, are combined in a special format and transmitted in biphase code to the surface buoy via a coaxial cable at 38 400 bits/second. The required high dynamic range was achieved by floating-point conversion of the geoacoustical data.

The output of the sensor is lowpass filtered (100 Hz anti-aliasing) and fed directly and via three additional amplifier stages of 18, 36, and 54 dB into a 4×4-channel multiplexer. For each channel these four signal levels are sampled at 600 Hz. The second multiplexer then uses a level detector and a priority encoder to select and hold that sample which is not yet saturating the subsequent (11+1)-bit fast A/D converter. The priority encoder passes on this information about the selected amplifier stage in the form of two other bits. The former (11+1) bit and these two bits represent the mantissa and the exponent of the sensor data (floating-point conversion), thus offering a dynamic range of 66+(3×18) = 120 dB. Together with a parity bit and another independent bit these (12+2) bits form the basic data word of 16 bits.

After three scanning cycles of the four basic sensors, twelve additional bits are available. Eleven of these bits are used to transmit digital information from the environmental sensors and check points, while the twelfth produces a framing and synchronization pattern.

For calibration purposes a stabilized ac current is injected into the calibration coil of the geophones for a fixed period whenever the OBS is switched on.

Table 1 summarizes the most important mechanical data of the OBS unit.

TABLE 1

TRIAXIAL SACLANTCEN OBS

Minimum height of the cylindrical container	12.5 cm
Maximum height (includ. central lid)	18 cm
Diameter of the container	50 cm
Total volume	25 500 cm^3
Total mass	41 kg
Total weight in air	402 N
Package density	1.6 g/cm^3
Total weight in water	152 N
Bearing pressure in water	775 N/m^2

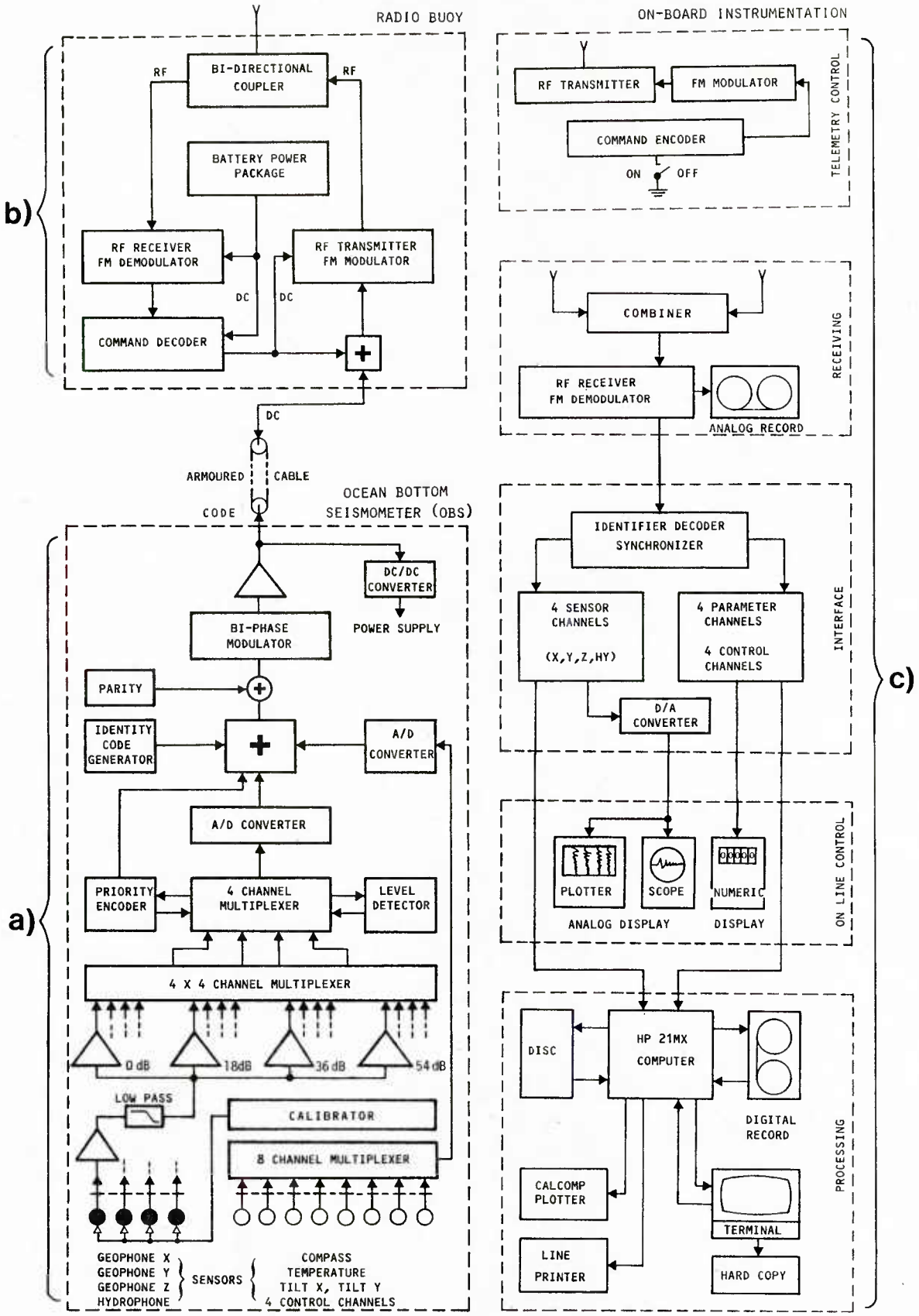

FIG. 4 ELECTRONIC BLOCK DIAGRAM
a. Ocean-bottom seismometer
b. Radio buoy
c. Onboard data handling

2.1.2 The radio buoy (Fig. 4b)

This surface unit contains:

- Rechargeable batteries to power the entire system for 16 h of data acquisition.
- FM-modulated VHF radio-transmitter (max. 10 W output).
- A standby radio receiver for power on-off commands.

2.1.3 On-board instrumentation (Fig. 4c)

The instrumentation comprises the five sections identified in the figure:

- A telemetry control unit to transmit the power on-off code to the radio buoy.
- A radio receiver that combines the signals from two antennas and feeds a standard sonobuoy receiving set. The output baseband signal is recorded on analogue magnetic tape and passed on to the interface unit.
- An interface to decode the data-stream (bit and word synchronization), thereby restoring the original sensor outputs to digital and analogue form.
- An on-line control unit to provide display and plot options for the geoacoustic data channels and numeric readouts for the auxiliary parameters.
- An acquisition and pre-processing system based on Hewlett-Packard 21MX computers with disc units and other peripherals. The disc-stored data are immediately available for display, plotting and pre-processing options and for transfer to digital magnetic tape.

2.2 Experimental Procedure

Figure 5 illustrates the experimental technique used to measure interface waves. A crucial point in the deployment was the need to ensure that the OBS was well coupled to the bottom and decoupled from vibrations of connecting cables and ropes. This was generally possible without the use of divers.

The receiving ship (normally the SACLANTCEN Research Vessel MARIA PAOLINA G.) anchored approximately 1 km from the radio buoy (greater distances would provoke disturbances in the VHF-telemetry link). During the experiment a source ship was used to deploy the explosive charges at successive ranges from the OBS. At each range the ship's engines were stopped and the explosive charge (45 g to 1450 g TNT) was lowered to the sea-floor and fired electrically. The pulse of the explosion was received

by a hydrophone below the source ship and transmitted to the receiving ship, where it was used to trigger the data acquisition on the computer. Although the use of explosive charges as broadband sources is a standard technique in underwater acoustic measurements it should be kept in mind that they contain extremely low energy per hertz within the very low-frequency band (1 to 6 Hz) used for these experiments.

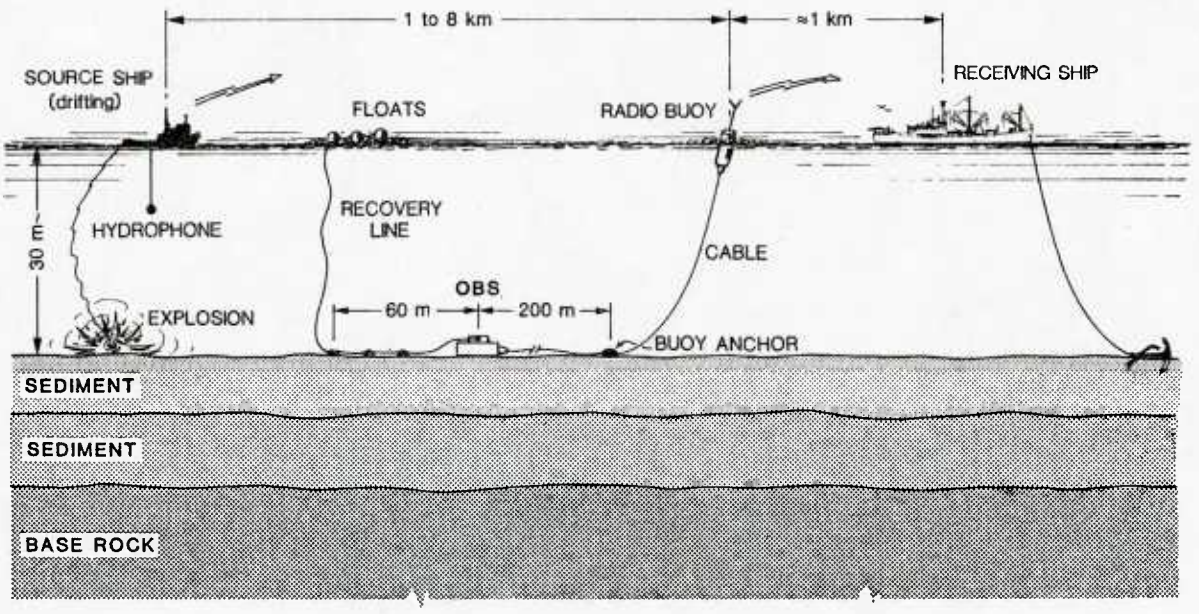

FIG. 5 DEPLOYMENT OF OBS SYSTEM AND EXPERIMENTAL PROCEDURE

3 PRESENTATION OF RESULTS

The results of the four experiments are presented in three standard forms: time/distance plots, dispersion analysis curves, and attenuation curves, as described in the following sections and illustrated in Fig. 6.

3.1 Time/distance plots (Fig. 6a)

The time/distance plots (or seismic sections) present the particle velocity seismograms as a function of their range. These plots allow specific conclusions to be inferred concerning the main group-velocities and frequencies involved in the wavelets propagating along the interface. Beyond this they offer an overview of the distribution of the seismograms in space and time, which is important in providing information on the general characteristics of the data.

Superimposed on each time/distance plot are lines of constant particle velocity, with the following common notation:

_____ Thick solid lines delineate the most evident contribution of the interface wave (65 m/s and 250 m/s on Fig. 6a).

------- A dashed line indicates a pronounced wavelet, to be identified as the first higher mode (145 m/s on Fig. 6a).

..... A dotted line indicates the arrivals of the direct water wave (1520 m/s on Fig. 6a).

_____ One or two thin solid lines indicate the direct p-wave arrivals, or even refracted p-wave arrivals, (1715 m/s, 2850 m/s on Fig. 6a). However, evidence for a refracted p-wave was found only in the experiment at site R.

All seismograms are low-pass filtered (10 Hz) to emphasize the lower frequency interface wavelets, on which higher frequency background noise was occasionally superimposed. Of course, this filtering degrades the detectability of the fast arrivals (water wave, p-wave), so these onsets were therefore determined separately from the unfiltered seismograms.

Generally two time/distance plots are presented for each run, one for the vertical and one for the radial particle velocity, thus representing the motion in the relevant vertical/radial plane. Furthermore, within each run all seismograms were subjected to the same post-amplification factor. Therefore it is not only possible to read the particle velocity in absolute units (by means of the 50 μm/s bar), but also to draw some conclusions about the degree of polarization of the interface wavelet in the vertical/radial plane.

The sizes of the explosive charges are indicated as black dots at the end of each seismogram trace, one dot standing for 180 g TNT. During a run the charge size had to be changed to prevent the shock pulse of the direct water arrival from damaging the OBS. This was done by choosing small charges at close ranges and, so as to emphasize the interface wavelet against the background noise, by increasing the charge size at long ranges. Occasionally the shockwave saturated the first part of the seismograms (as seen in Fig. 6a). This is because the signals were post-amplified in order to emphasize the interesting interface wavetrains.

3.2 Group-velocity dispersion analysis curves (amplitude contours) (Fig. 6b)

Dispersion analysis of the seismograms gives information on the mode structure of the interface waves, showing how they have been split by the layering of the bottom or by the depth-dependence of the bottom parameters. This was done by applying the "multiple-filter technique" <15,16,17> described in App. B.

The product of such an analysis is the dispersion curve in the form of a (constant) amplitude contour in the group-velocity/frequency domain. These amplitude contour plots are normalized to 99 dB as maximum value; the range, which is from 80 dB to 98 dB, is displayed in 3 dB intervals. To facilitate a comparison of the results at different locations all but one of the amplitude contour plots in this report use identical axes of 75 to 275 m/s and 1 to 6 Hz.

In general, for each run, a dispersion analysis of the vertical and radial particle velocity seismograms was performed for an event at about 1.8 km range from the OBS. These seismograms are marked by an arrow "→" in the corresponding time/distance plots.

The practical value of such dispersion analyses (obtained already from one OBS) is that they may serve as input information for modelling studies, as has been demonstrated in <18> and <19> for example.

3.3 Attenuation curves (Fig. 6c)

The third quantity investigated here is the attenuation of the interface wave. The analysis is applied to the vertical and the radial particle velocities separately, and the result is plotted in the form 10 log E** vs range (attenuation curve). The double asterisk (**) is used here to indicate that the energy has been normalized both with respect to charge size (mass $^{4/3}$-law) and geometrical spreading (1/range). The software to obtain the wavelet energy, along with the formulae to normalize the values, are presented in App. C.

The attenuation coefficients derived from the slope of the attenuation curve are listed in the text. They are to be considered as average values over the relevant frequency interval, 1.5 to 5.3 Hz, of the entire wavelet; in other words, an average over the modes involved.

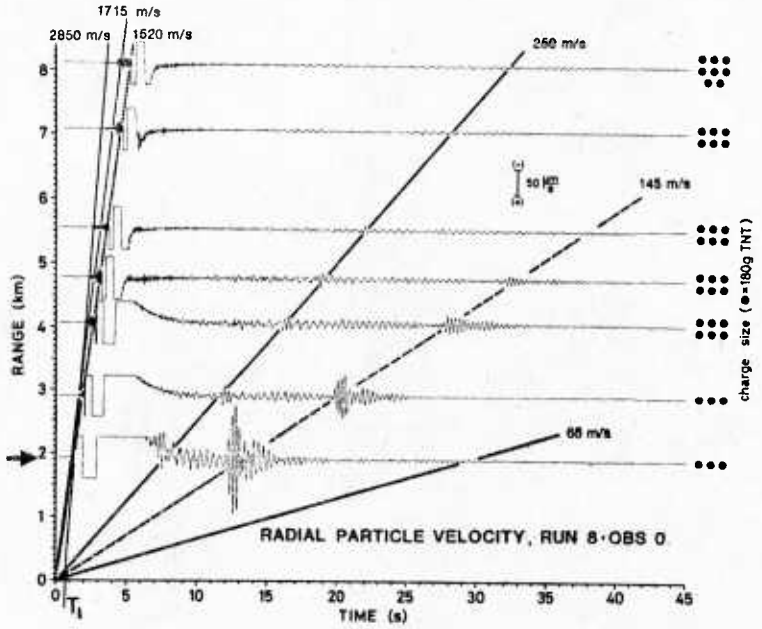

a)

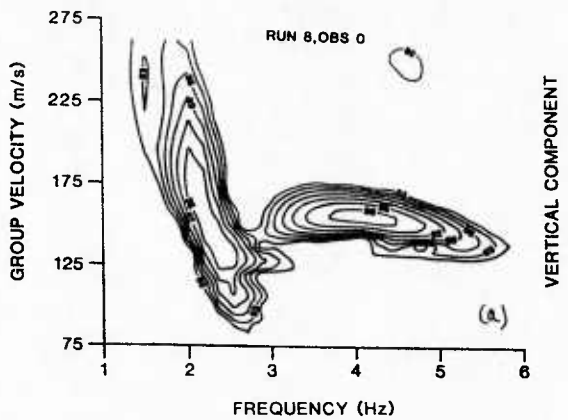

b)

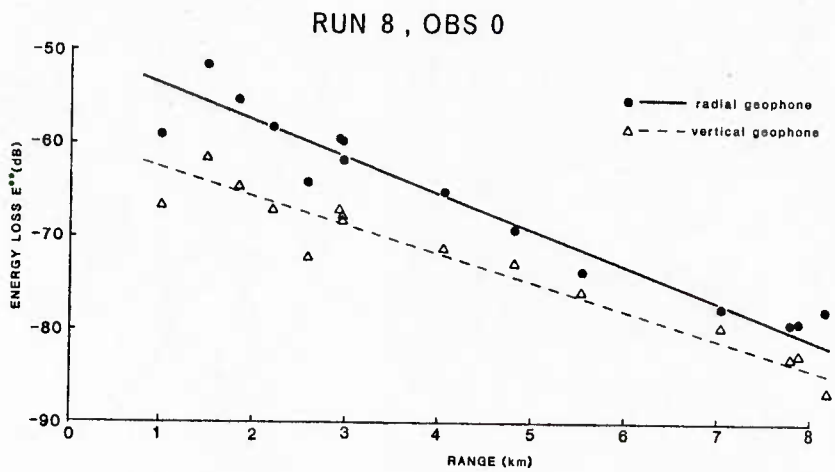

c)

FIG. 6 METHODS OF PRESENTING EXPERIMENTAL RESULTS
a. Time/distance plot
b. Amplitude contours (group-velocity dispersion analysis)
c. Attenuation curve

4 EXPERIMENTAL RESULTS

4.1 Experiment P

Table 2 summarizes conditions at site P (Fig. 1), where two runs were performed.

TABLE 2

CONDITIONS AT SITE P

ID	Date	Position Long/Lat	Runs	Bottom Type	Water depth	OBS deployed
P	July 79	Off Viareggio 10°68'E 43°52'N	# 2 # 3	Regularly layered sediments	20 m at OBS location	1

4.1.1 Run 2

Figure 7 shows the two time/distance plots of 15 events during run 2, when measurements were conducted up to 5 km range. The first pronounced arrivals with high-frequency oscillations are associated with the direct water wave, having a sound speed of 1536 m/s (average value calculated from XBT measurements). The low-frequency interface waves are characterized by the long (up to 20s), narrow-band and dispersed wave trains included within the two solid lines. The initial part of the wave trains contains 1.5 to 2 Hz oscillations and a group velocity of 240 m/s, whereas the tail is marked by 4 to 5 Hz oscillations and a group velocity of about 75 m/s. This means that the dispersion is normal: lower frequency oscillations (or larger wavelengths) propagate faster than higher frequency ones (or shorter wavelengths).

Since the wavelength of the interface waves is related to its penetration into the sediment, the observed dispersion implies that there is an increase of (sediment-) consolidation with increasing depth, as one would also expect. Furthermore, owing to the strong connection between the velocities of the interface wave and the shear wave (see Ch. 1), we can state that the shear-wave velocity gradient is positive.

The dashed line between the two solid lines in Fig. 7 corresponds to a group velocity of 185 m/s. The associated wavelet is weakly dispersed and must be attributed to a higher mode. This is also indicated by the amplitude contour plots in Fig. 8, which are the results of a dispersion analysis performed for the events marked by arrows in Fig. 7. The amplitude distribution of the vertical component (Fig. 8a) reveals the coexistence of two modes, with a strongly prevalent fundamental mode (lowest group velocity). On the other hand, the radial component (Fig. 8b) indicates contributions from three modes, with a strongly prevailing first mode.

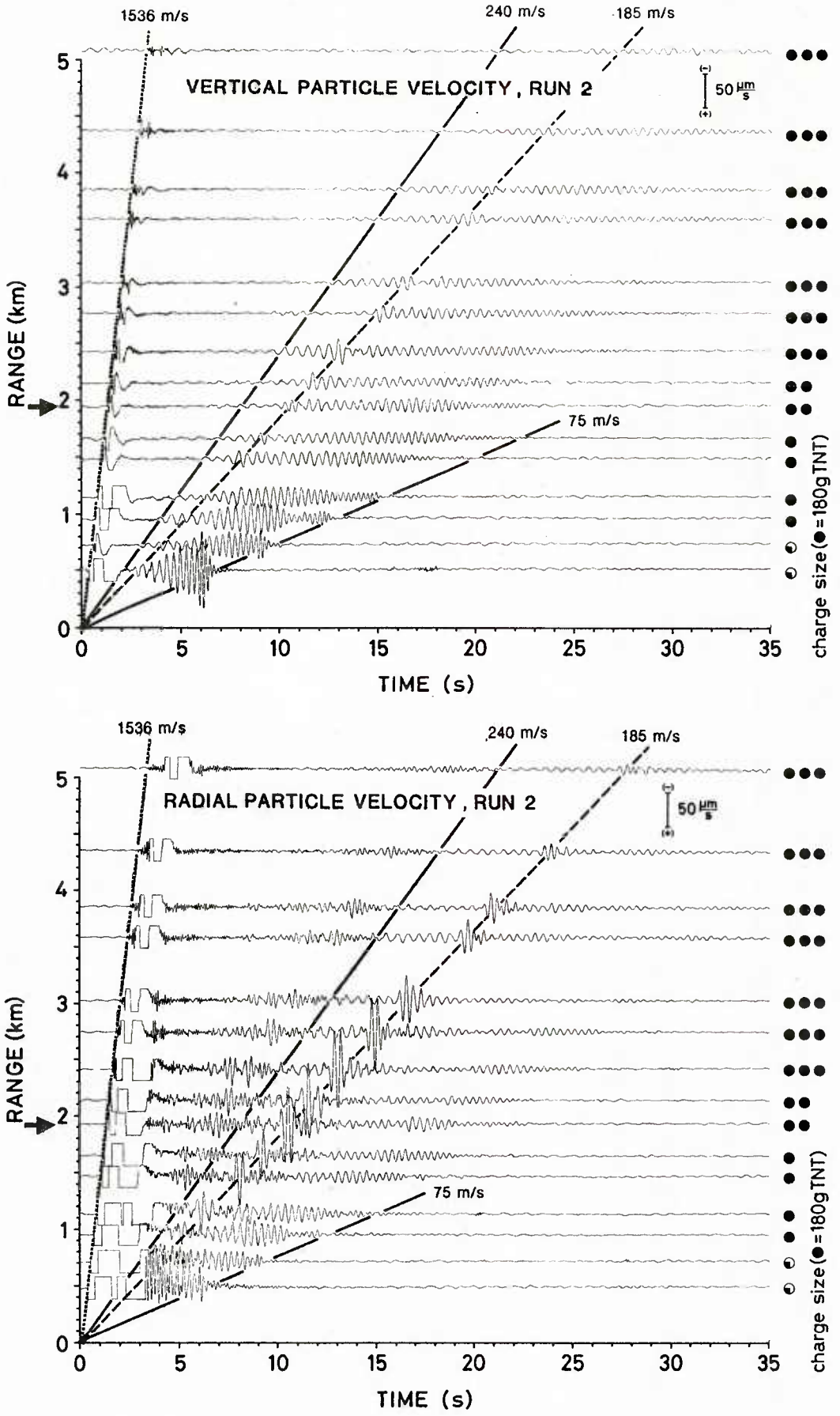

FIG. 7 SITE P, RUN 2: TIME/DISTANCE PLOTS
a. Vertical component
b. Radial component

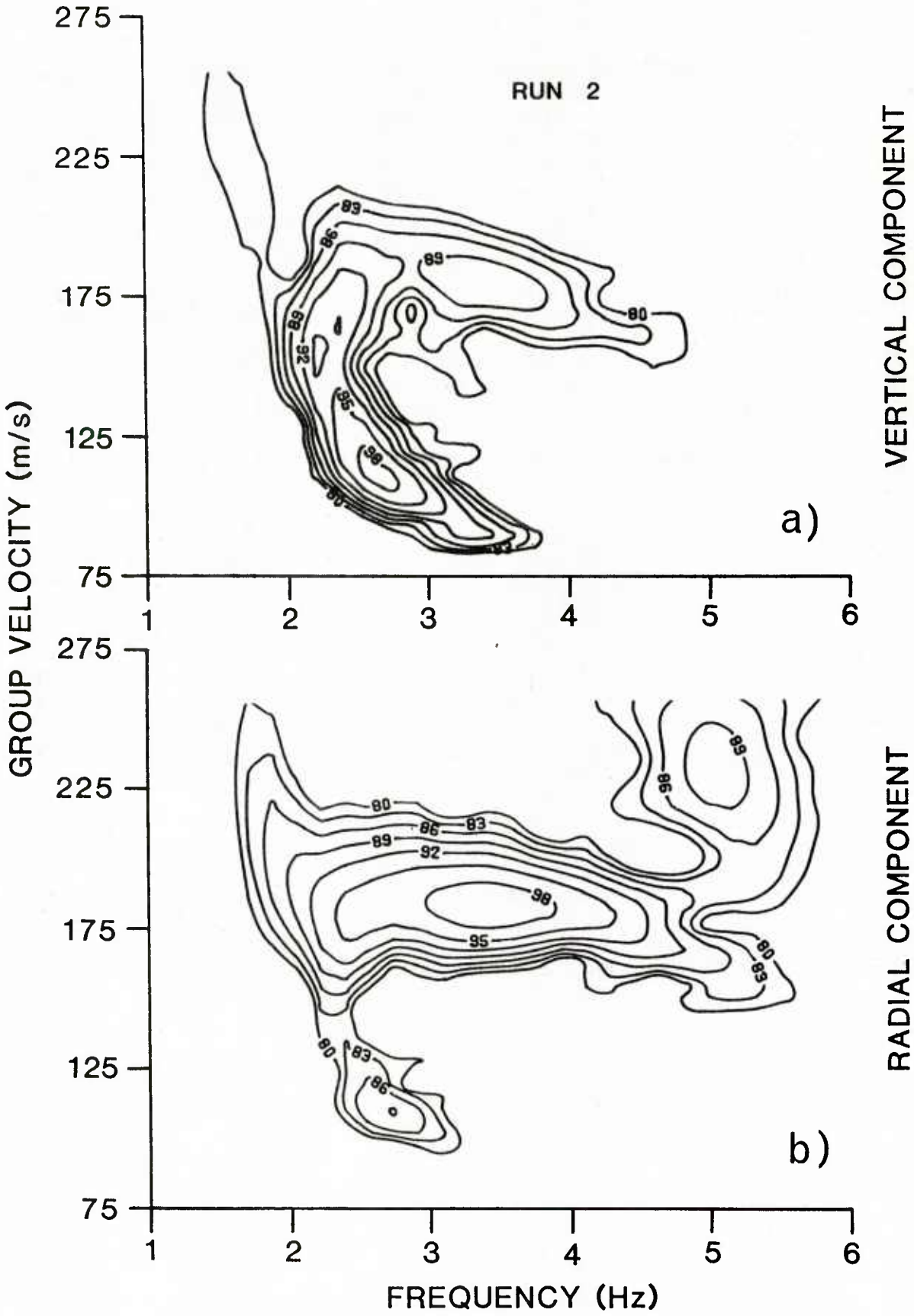

FIG. 8 SITE P, RUN 2: AMPLITUDE CONTOURS FROM EVENT "→" OF FIG. 7
a. Vertical component
b. Radial component

The relevant hodographs in the radial/vertical plane and the associated seismograms are shown in Fig. 9b and 9a, respectively. The results shown are confined to the interface-wave portion of interest. The time scale is divided into fourteen 1-second intervals (A to N). As is seen in Fig. 9b, the wavelet in time window B (corresponding to the first mode, 185 m/s) is associated with a horizontally aligned ellipse of high eccentricity, whereas the fundamental mode (intervals E to K) is associated with vertically aligned, low-eccentricity orbits. In each case the sense of the motion is prograde, a fact that is also inferred from the corresponding radial/vertical phase contour plots. These phase plots reveal, further, that the weak second mode is associated with retrograde polarized motion.

The existence of Rayleigh and Scholte waves having propagation modes with prograde or retrograde particle motion has been demonstrated on land and on the ocean bottom <6,20,21,22>. Recently published propagation data from a shore belt of the North Sea <23> describe a situation in which the tail of the wavetrain (fundamental mode at 100 m/s) consisted of prograde particle motions, while the front (first mode at 200 m/s) originated from retrograde motions.

Another phenomenon, which will be only briefly described, concerns the "forerunners" of the interface wave. These are the relatively conspicuous and long-lasting particle motions between the decay of the water wave and the onset of the interface wave in Fig. 7, which are also to be seen in the transverse component. Brocher et al <24> report from similar experiments a (SV) shear wavelet of 3 Hz with clearly discernible constant-velocity onset of 420 m/s. The present results are somewhat different in that they do not reveal significant vertical motion and a clear (3 Hz) wavelet. However, they also suggest waves with dominant shear character; but the exact wave mode is not yet fully understood.

The two attenuation curves in Fig. 10 describe the attenuation along run 2 of the vertical and radial components for the entire wavetrain. The following attenuation coefficients taken from the slopes of the straight regression lines are determined from run 2:

vertical component: $\alpha_V \approx 5$ dB/km (solid line on Fig. 10),
radial component: $\alpha_r \approx 3$ dB/km (dashed line on Fig. 10).

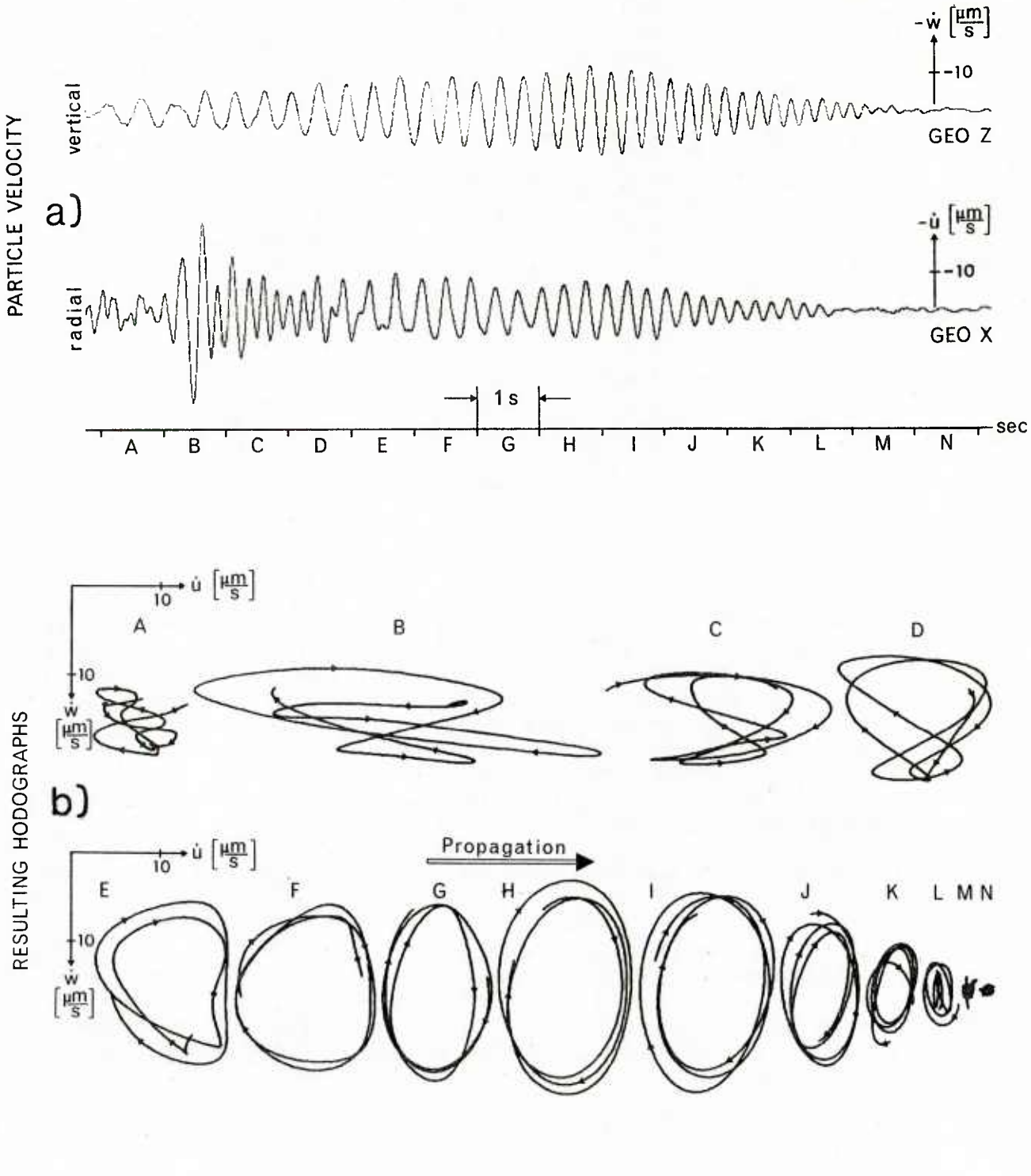

FIG. 9 SITE P, RUN 2: SEISMOGRAMS AND RESULTING HODOGRAPHS

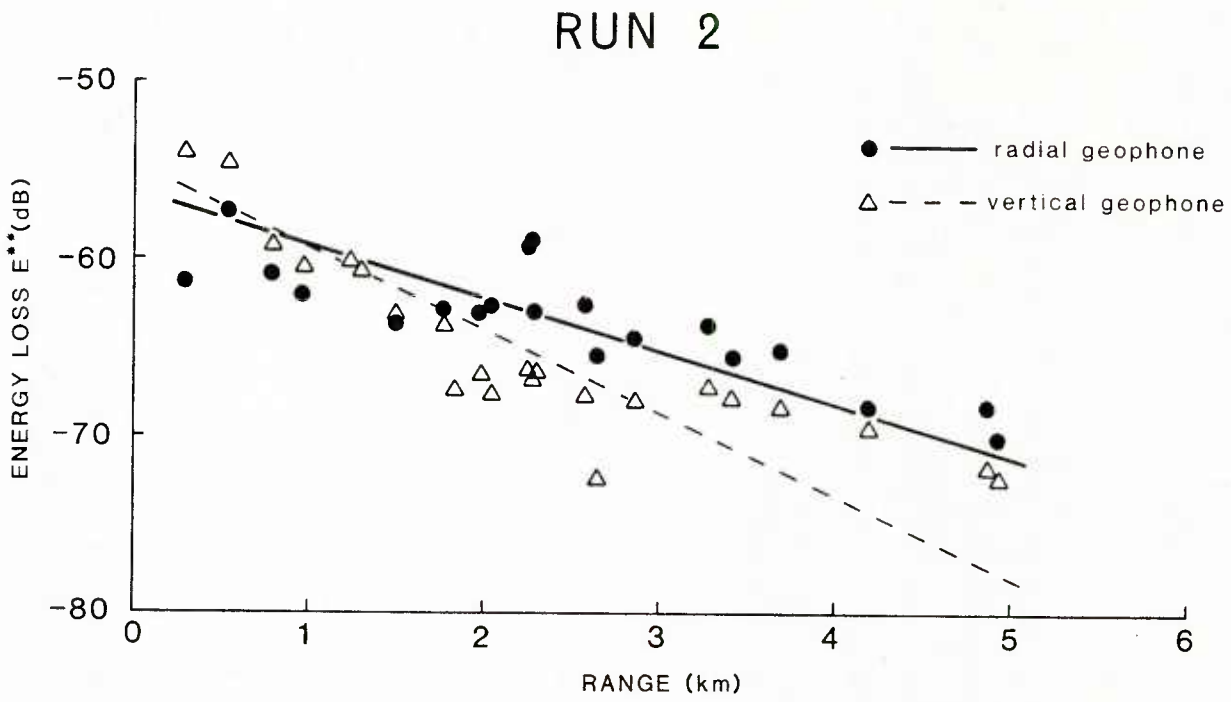

FIG. 10 SITE P, RUN 2: ATTENUATION CURVES

4.1.2 Run 3

Figure 11 shows the time/distance plots obtained from run 3. Compared with run 2, the interface wavetrains of the vertical and radial component have more regular amplitude and frequency characteristics and are less likely to split into several wave groups. The superimposed wavelet (185 m/s) is much less pronounced and is subject to a quite substantial normal dispersion. These significant features are also confirmed by the amplitude contour plots of Fig. 12, calculated for an event at 1.8 km distance. These also reveal a slight frequency shift of 0.5 Hz towards the lower frequencies of the fundamental and first mode.

The attenuation curves for run 3, shown in Fig. 13, give the following attenuation coefficients:

vertical component: $\alpha_V \approx 10$ dB/km,
radial component: $\alpha_r \approx 6$ dB/km.

These attenuation coefficients are much higher than those from run 2, which indicates that the composition and/or the layering along these propagation paths are different.

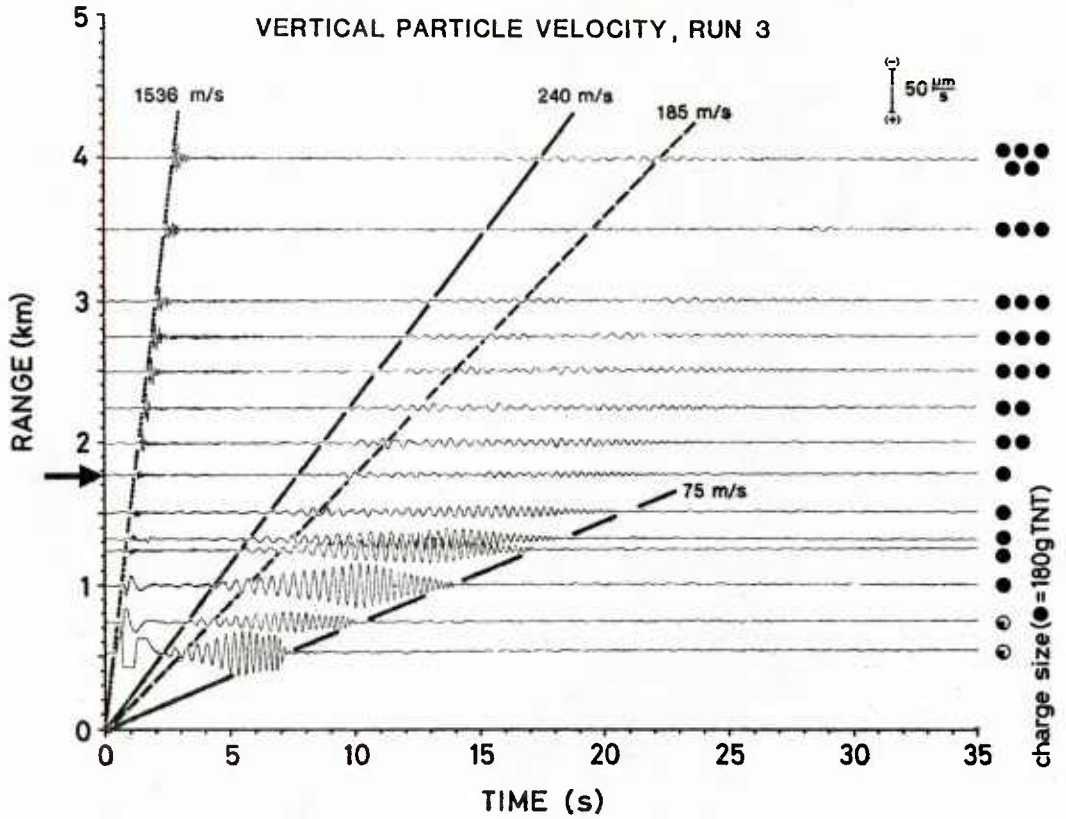

a)

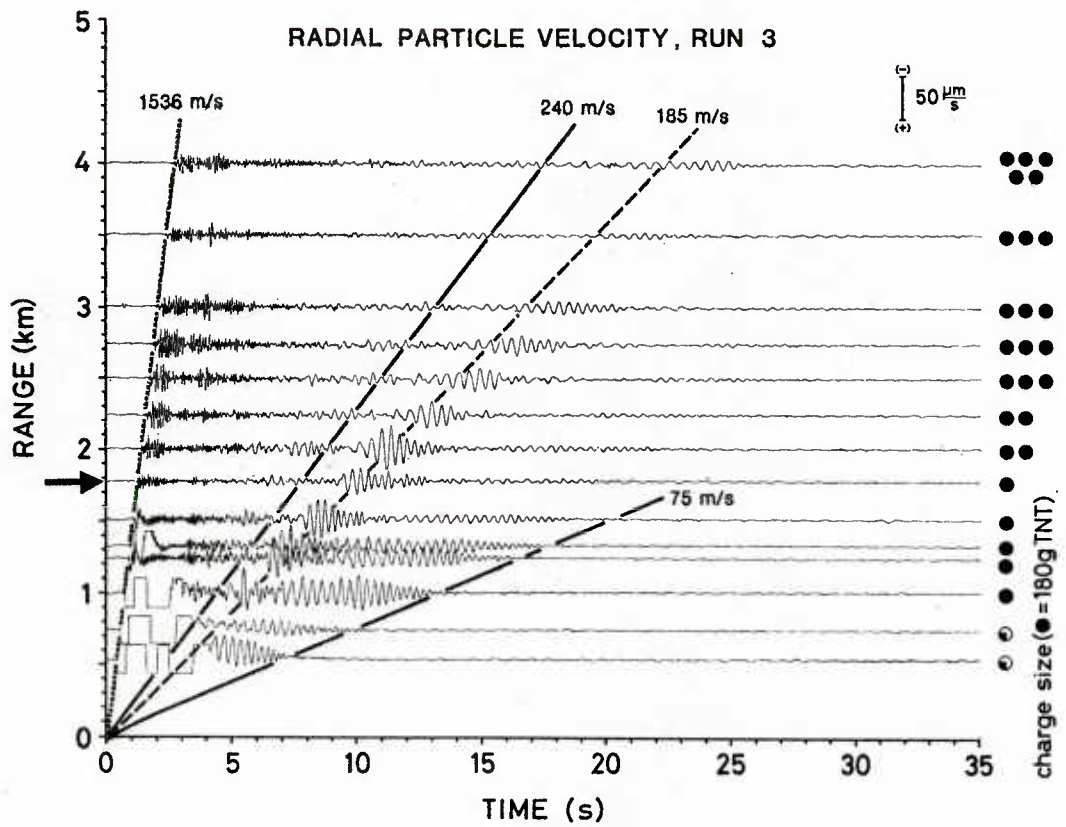

b)

FIG. 11 SITE P, RUN 3: TIME/DISTANCE PLOTS
a. Vertical component
b. Radial component

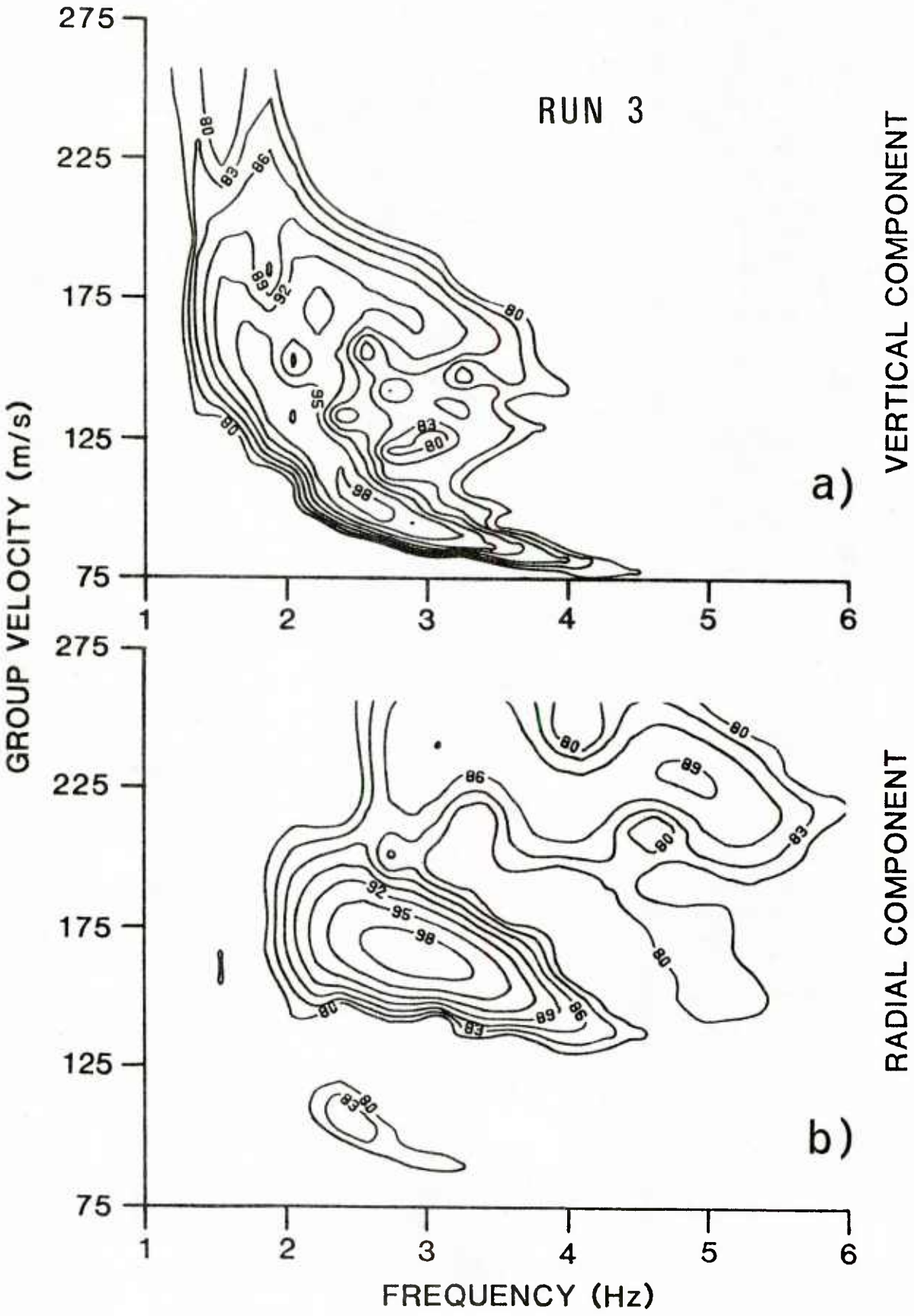

FIG. 12 SITE P, RUN 3: AMPLITUDE CONTOURS FROM EVENT "→" OF FIG. 11
a. Vertical component
b. Radial component

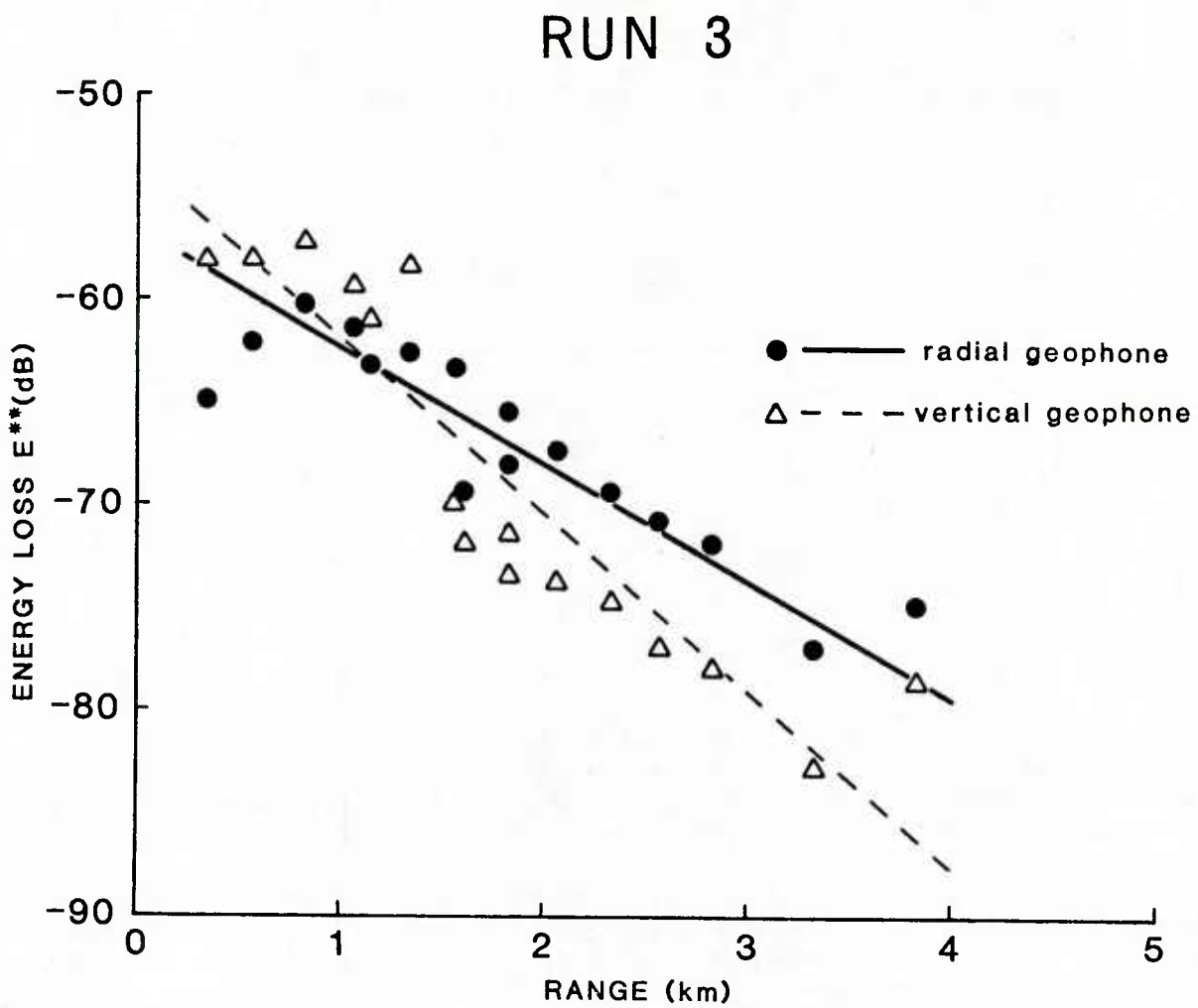

FIG. 13 SITE P, RUN 3: ATTENUATION CURVES

4.2 Experiment M

Table 3 summarizes conditions at site M (Fig. 1), where two runs were performed.

TABLE 3

CONDITIONS AT SITE M

ID	Date	Position Long/Lat	Runs	Bottom Type	Water depth	OBS deployed
M	Sep 79	Off Livorno 10°11'E 43°30'N	# 5 # 6	Irregularities relatively hard	25 m	1

It was intended to carry out this experiment on a hard homogeneous sea-floor in contrast to that of the previous site. For the strongly idealized case of a homogeneous rock half-space, theory predicts a relatively high phase-velocity, no dispersion, and a retrograde particle motion <3>.

The geological and bathymetric charts of the upper Tyrrhenian Sea do not indicate any extended area where the hard basement rock or consolidated sediments emerge at the sea-floor surface. The few existing zones with a consolidated sedimentary sea bottom are generally characterized not only by a relatively rough surface (grooves and outcrops) but also by a quite complicated internal structure (inclined and irregular layering). Although, from this, one could not expect optimal propagation conditions, it was decided to deploy the OBS on the shoals off Livorno (Leghorn), which also gave the opportunity to track nearby passing ships and make ambient-noise measurements (not reported here).

The analysis of data from this site was limited to time/distance plots of the vertical particle velocity and, for run 5 only, to the corresponding dispersion analysis curve. The time/distance plots of the radial component are omitted because these interface wavetrains could hardly be distinguished against the background; this might be due to bad coupling of the OBS to the sea-floor. Attenuation curves and coefficients were not calculated, because the limited number of seismograms is not sufficient to yield reliable results. Figures 14 and 15 plot the data from run 5 and Fig. 16 plots the data from run 6.

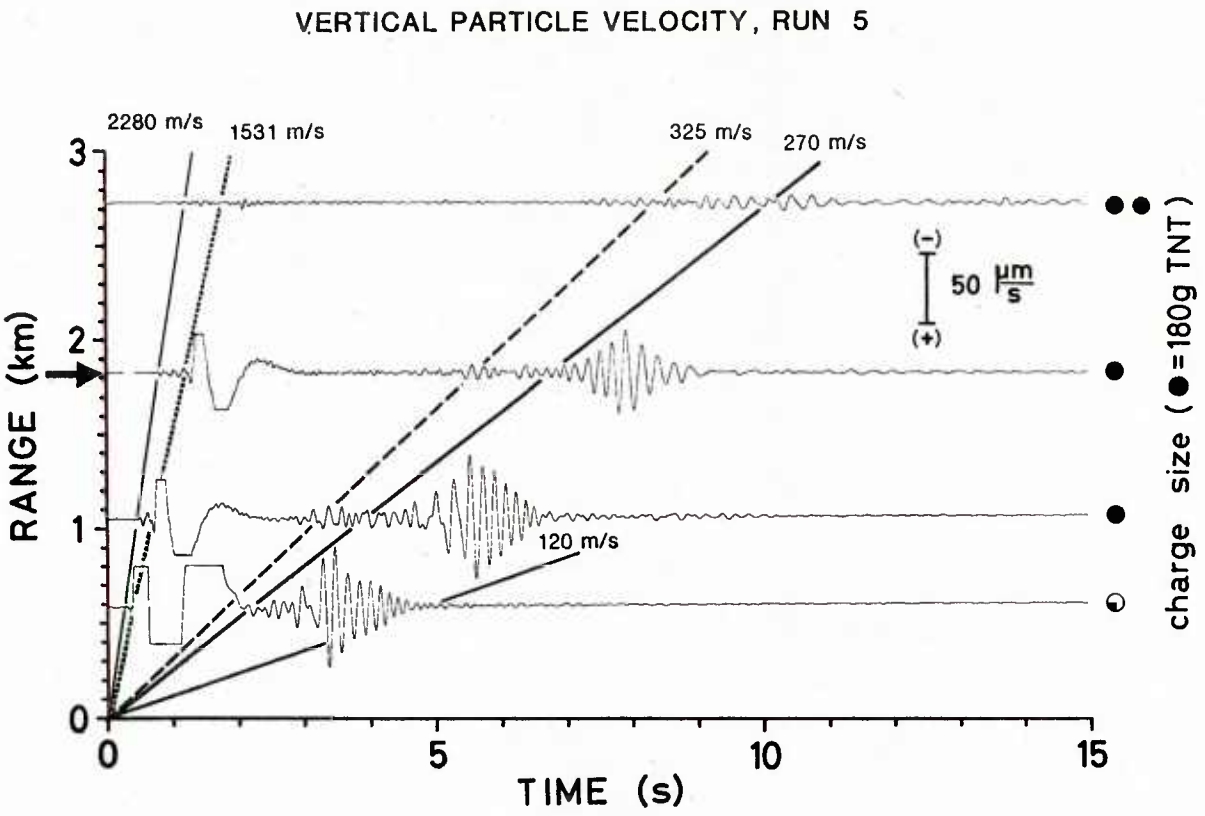

FIG. 14 SITE M, RUN 5: TIME/DISTANCE PLOTS
Vertical component only

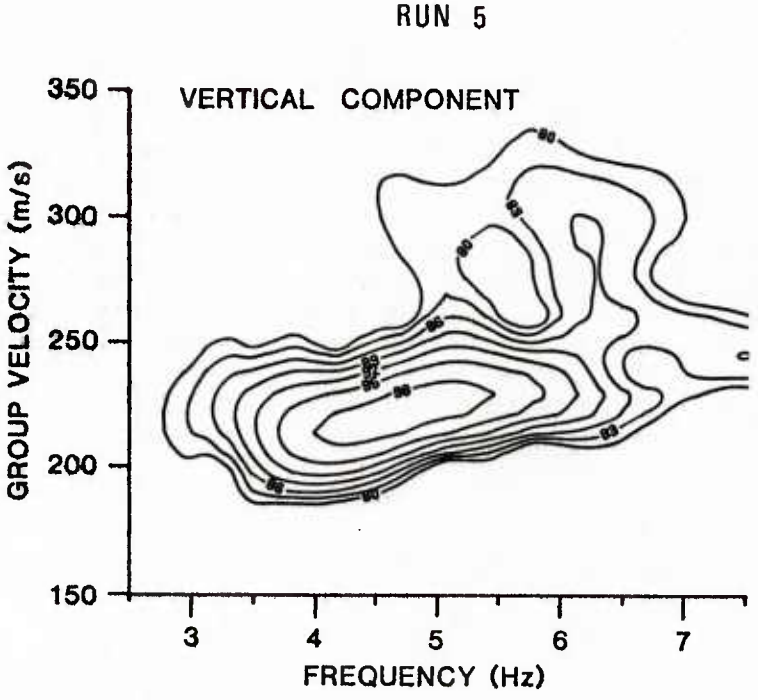

FIG. 15 SITE M, RUN 5: AMPLITUDE CONTOURS
Vertical component, from event "→" of Fig. 14

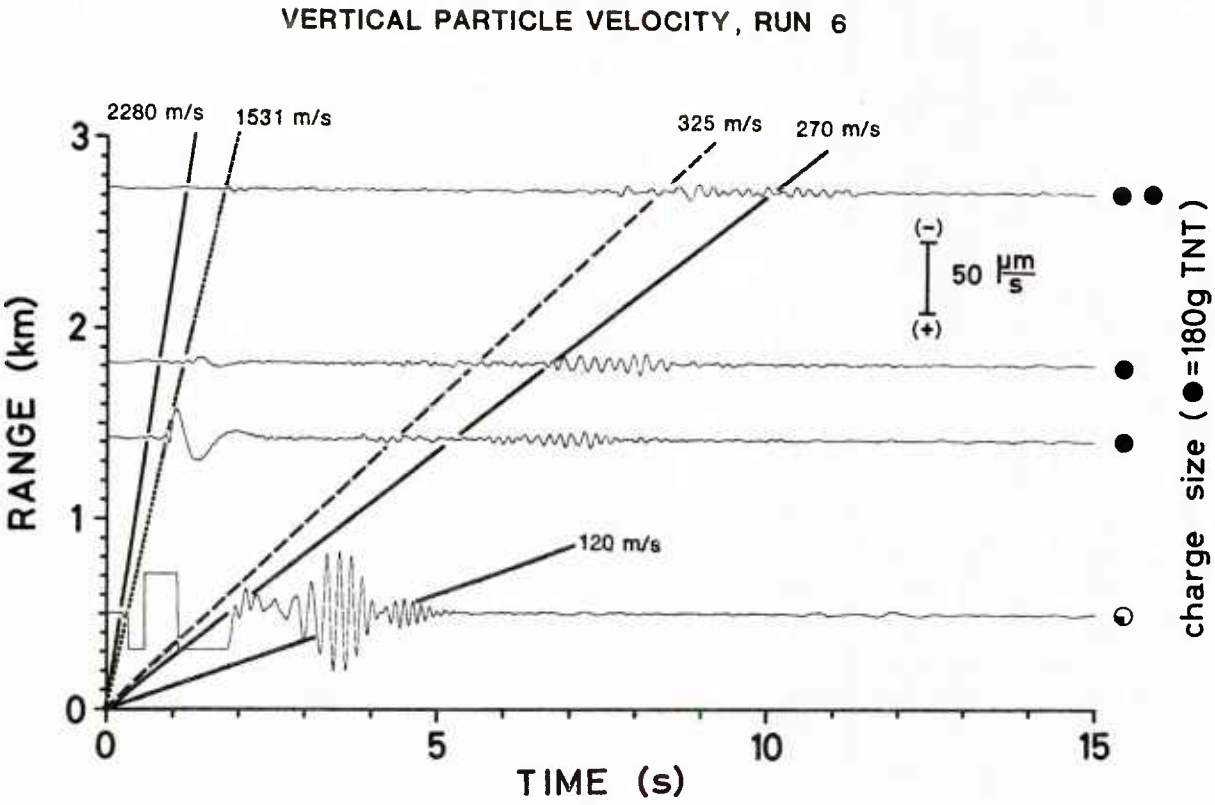

FIG. 16 SITE M, RUN 6: TIME/DISTANCE PLOTS
Vertical component only

The seismograms of Figs. 14 and 16 show that the interface wave velocities range from about 120 m/s to 270 m/s and that the wavetrains are weakly dispersed. As expected for the harder bottom, these velocities are clearly higher than those observed at site P. Another particular wavelet, with an even higher velocity of about 300 m/s is also indicated; its existence is proved by the amplitude contour of Fig. 15. This plot also shows the extremely weak dispersion of the fundamental mode, which is even slightly anomalous. The corresponding contour plots for the phase between the radial and vertical velocity component (not shown here) demonstrated the existence of a purely retrograde particle motion: an infrequently observed example of a counterclockwise polarized fundamental mode. The first mode, however, is clockwise polarized.

Thus, although the deployment off Livorno did not result in a drastic increase of the interface wave velocities, it was a first step towards obtaining results from a hard bottom, showing almost no dispersion and a retrograde particle motion. It was also the first time that a distinct arrival of the direct p-wave (2280 m/s) [head wave] was noticed ahead of the water wave (1531 m/s).

4.3 Experiment G

Table 4 summarizes conditions at site G (Fig. 1), where one run was performed.

TABLE 4

CONDITIONS AT SITE G

ID	Date	Position Long/Lat	Run	Bottom Type	Water depth	OBS deployed
G	Sep 80	Off M. di Carrara 9°58.2'E 43°57.7'N	# 7	Unconsolidated sediments	20 m	2 at 550 m distance

In September 1980 the two OBS were deployed southeast of Tino Island, off Marina di Carrara, where the sea floor consists of unconsolidated sediments. The two OBS stations were separated by about 550 m (not in scale on Fig. 1). The measurements were conducted on the bearing of 296° along which the two OBS (OBS 0 and OBS 1) were aligned. This technique of using two OBS gives the possibility of accurately calculating the seismic wave attenuation and, in principle, also the phase velocity. The seismograms obtained from the two OBS stations are compiled in two overlapping data sets: 7(A) and 7(B).

4.3.1 Run 7(A)

Figure 17 shows the time/distance plots of seismograms recorded by the nearer OBS 1 and Fig. 18 shows the same events recorded by the more distant OBS 0. The seismograms of the vertical component (Figs. 17a, 18a) show a relatively compressed, narrow-band wavetrain (interpreted as interface wave) with normal dispersion. At ranges beyond 1 km the decay of the wavetrain is characterized by 3 to 4 Hz oscillations with propagation velocity of about 78 m/s. At very short range even 5 to 6 Hz oscillations with velocities down to 50 to 60 m/s can be discerned. A comparison of these frequency/velocity combinations with those from site P (see Figs. 7 and 11) indicates that the top layers of the sea-floor are obviously much "softer" or "slower" at site G.

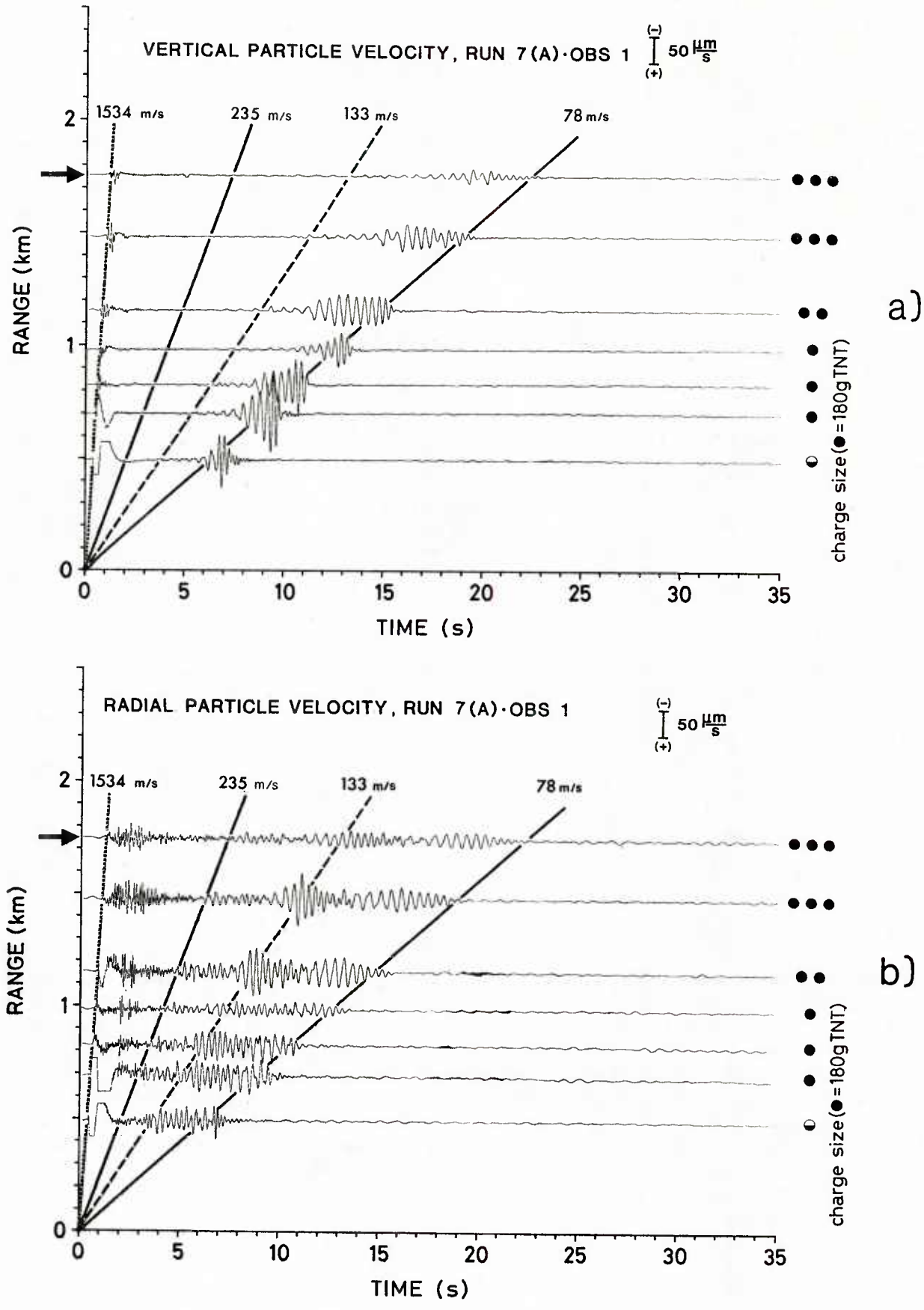

FIG. 17 SITE G, RUN 7(A): TIME/DISTANCE PLOTS FROM CLOSE OBS
a. Vertical component
b. Radial component

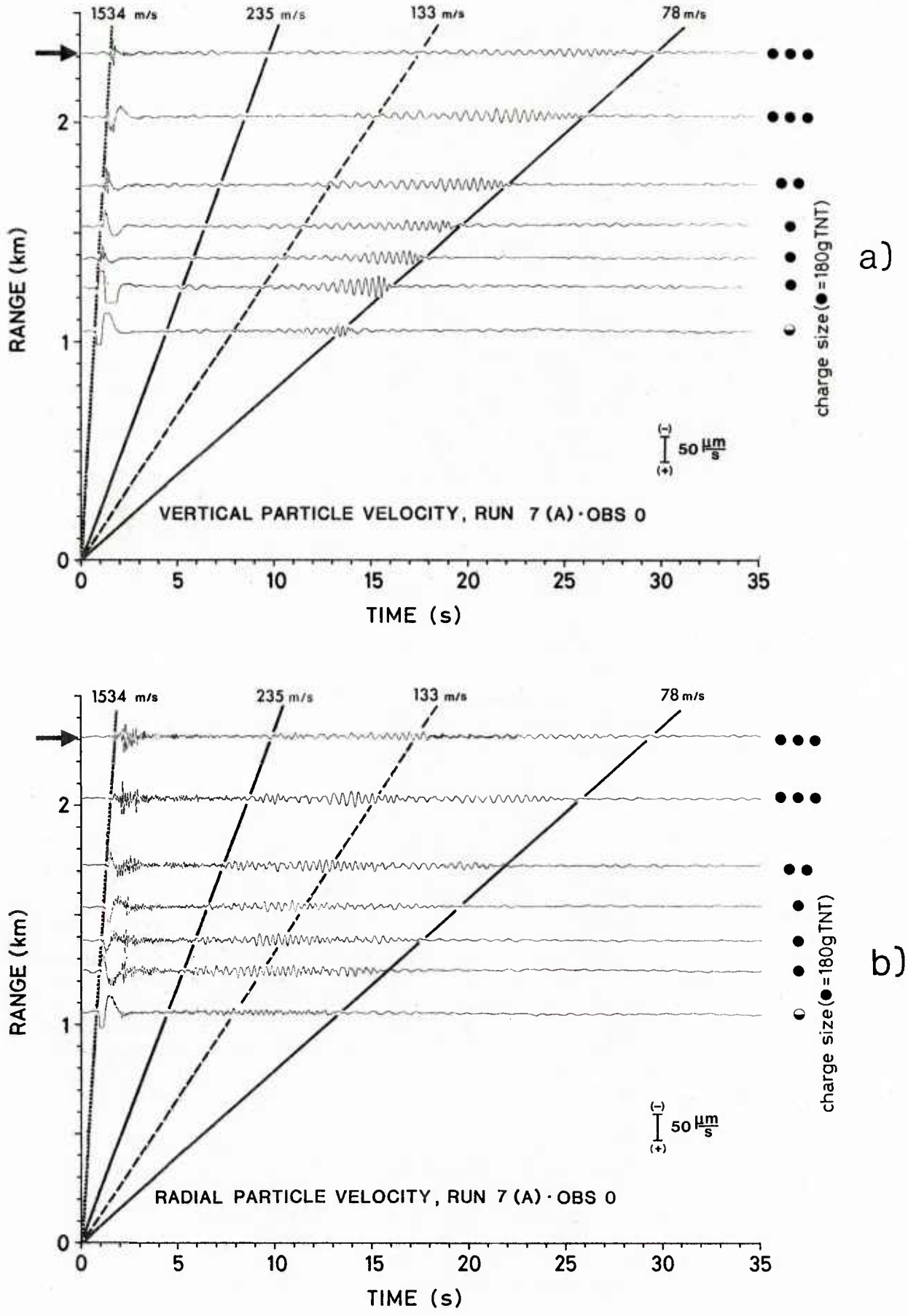

FIG. 18 SITE G, RUN 7(A): TIME/DISTANCE PLOTS FROM DISTANT OBS
a. Vertical component
b. Radial component

The seismograms of the radial components (Figs. 17b and 18b) also show the compressed, narrow-band wavetrain already indicated in the vertical motion. In addition, they show another pronounced wavelet propagating at 133 m/s (dashed line). Furthermore, the energy propagating with group-velocities between 235 m/s and the just-mentioned wavelet indicate another (strongly dispersed) mode.

The corresponding amplitude contours from a dispersion analysis offer more insight into the modal structure of the seismograms. These contours are reproduced in Fig. 19 for an event at 1.75 km distance, recorded by OBS 1, and in Fig. 20 for the same event, recorded by OBS 0, 2.3 km away. A comparison of the amplitude distributions of the vertical component (Figs. 19a and 20a) draws attention to a strongly dominating fundamental mode that has almost no dispersion above 2 Hz. A high attenuation of this mode above 3 Hz can be seen, but also a marked congruence of the branches below that frequency. The dispersion characteristic of the fundamental mode indicates that even the deepest penetrating large-wavelength oscillations down to about 2 Hz do not suggest any significant change in the bottom parameters. In other words: the depth-gradient of the shear parameters is quite moderate and smooth, at least down to the critical penetration depth at which the wavelength, λ_c, exceeds the sediment thickness.

This wavelength, λ_c, can be estimated by knowledge of the phase velocity, c_{ph}, at the frequency, f_c , below which the dispersion branch starts to change more drastically, in this case at about 2 Hz:

$$\lambda_c = c_{ph}/f_c \quad .$$

Phase velocities could not be determined in this experiment because the distance between the two OBSs was too great to obtain significant coherence values and therefore reasonable phase correlations.

In another recent experiment (not discussed in this report) where, however, the group-velocity at 2 Hz was 140 m/s instead of 85 m/s, the phase-velocity at 2 Hz has been estimated to be 290 m/s. Thus, taking account of the differences in the group-velocity, a value of some 180 to 200 m/s for the phase-velocity may be concluded, and therefore a sediment thickness of 90 to 100 m.

In contrast to the just-discussed fundamental mode, the first and second modes are not pronounced in the vertical component, whereas the radial component is significant enough to compete with that of the fundamental mode. Both the higher modes are obviously much more affected by dispersion than is the fundamental mode, due to their steeper dispersion curves between 2 and 4 Hz. The degree of congruence and mutual similarity of these mode patterns is again very high and reflects the quality of the measurements.

Regarding the particle hodographs (not shown for this experiment), it is again necessary to attribute vertically aligned ellipses to the fundamental mode and horizontally oriented ellipses (with high eccentricity) to the first and second modes. From the corresponding phase contours it appears that the fundamental and the first mode are again characterized by a prograde particle motion, while that of the weaker second mode is partly prograde (above 3.5 Hz) and partly retrograde (below 3.5 Hz).

4.3.2 Run 7(B)

The seismograms from the second data set, run 7(B), are represented in Figs. 21 and 22, and the corresponding contour plots in Figs. 23 and 24. The seismograms in the time/distance plots of Figs. 1 and 22 are very similar to those of run 7(A), as expected. Some of the interface wavelets seem to be somewhat more developed.

The associated amplitude contours also confirm previous findings, for example the attenuation of the higher frequencies in the fundamental mode. The slightly more confusing amplitude distribution in Fig. 24b is due to an enhanced background noise in this case.

The two regression lines describing the attenuation of the interface waves in the vertical and radial component are plotted in Fig. 25. The analysis is based on both data sets 7(A) and 7(B); the two relatively high attenuation coefficients are:

vertical component: $\alpha_V \approx 9$ dB/km,
radial component: $\alpha_r \approx 10$ dB/km.

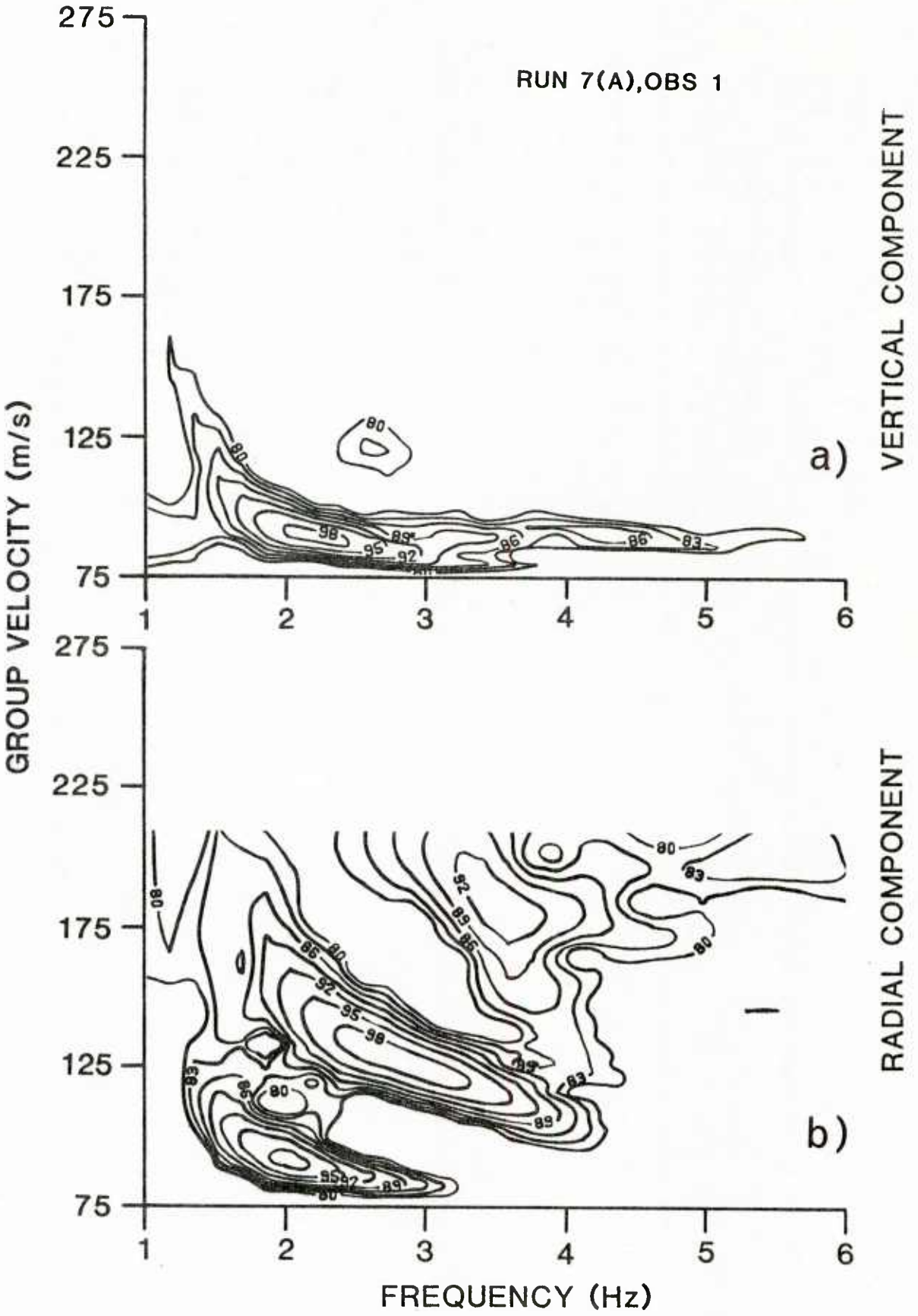

FIG. 19 SITE G, RUN 7(A): AMPLITUDE CONTOURS FROM EVENT "→" OF FIG. 17 (close OBS)
a. Vertical component
b. Radial component

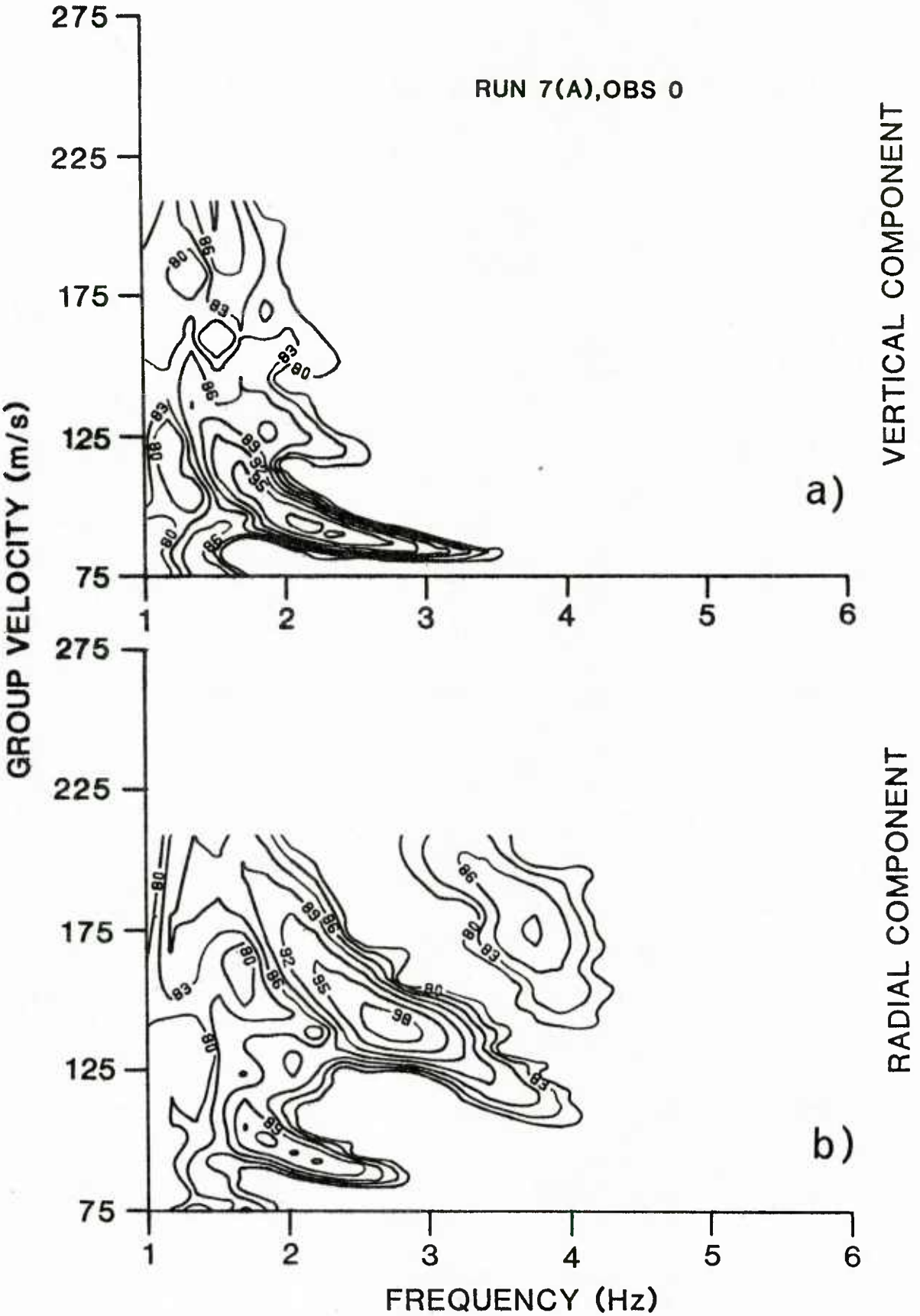

FIG. 20 SITE G, RUN 7(A): AMPLITUDE CONTOURS FROM EVENT "→" OF FIG. 18 (distant OBS)
a. Vertical component
b. Radial component

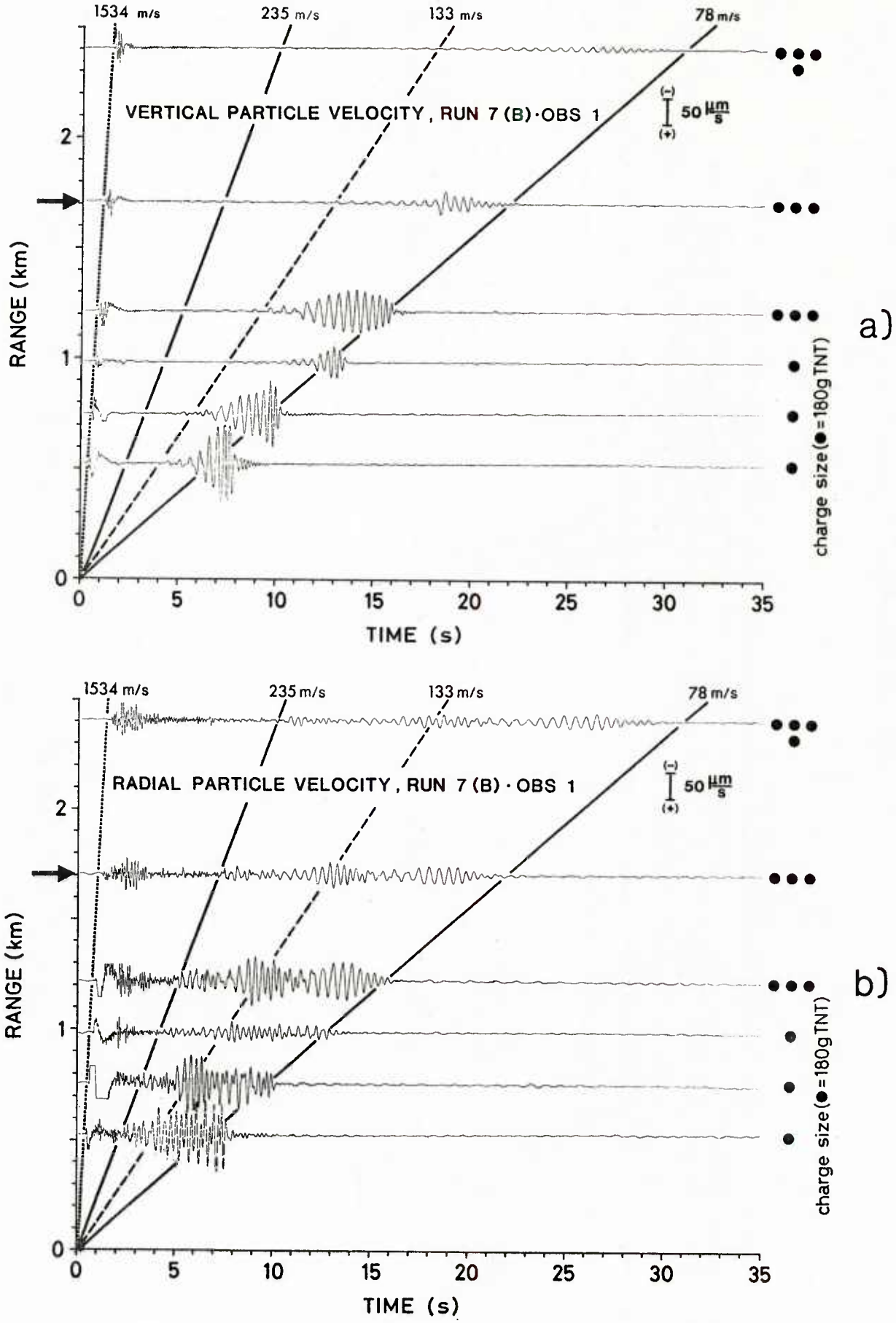

FIG. 21 SITE G, RUN 7(B): TIME/DISTANCE PLOTS (close OBS)
a. Vertical component
b. Radial component

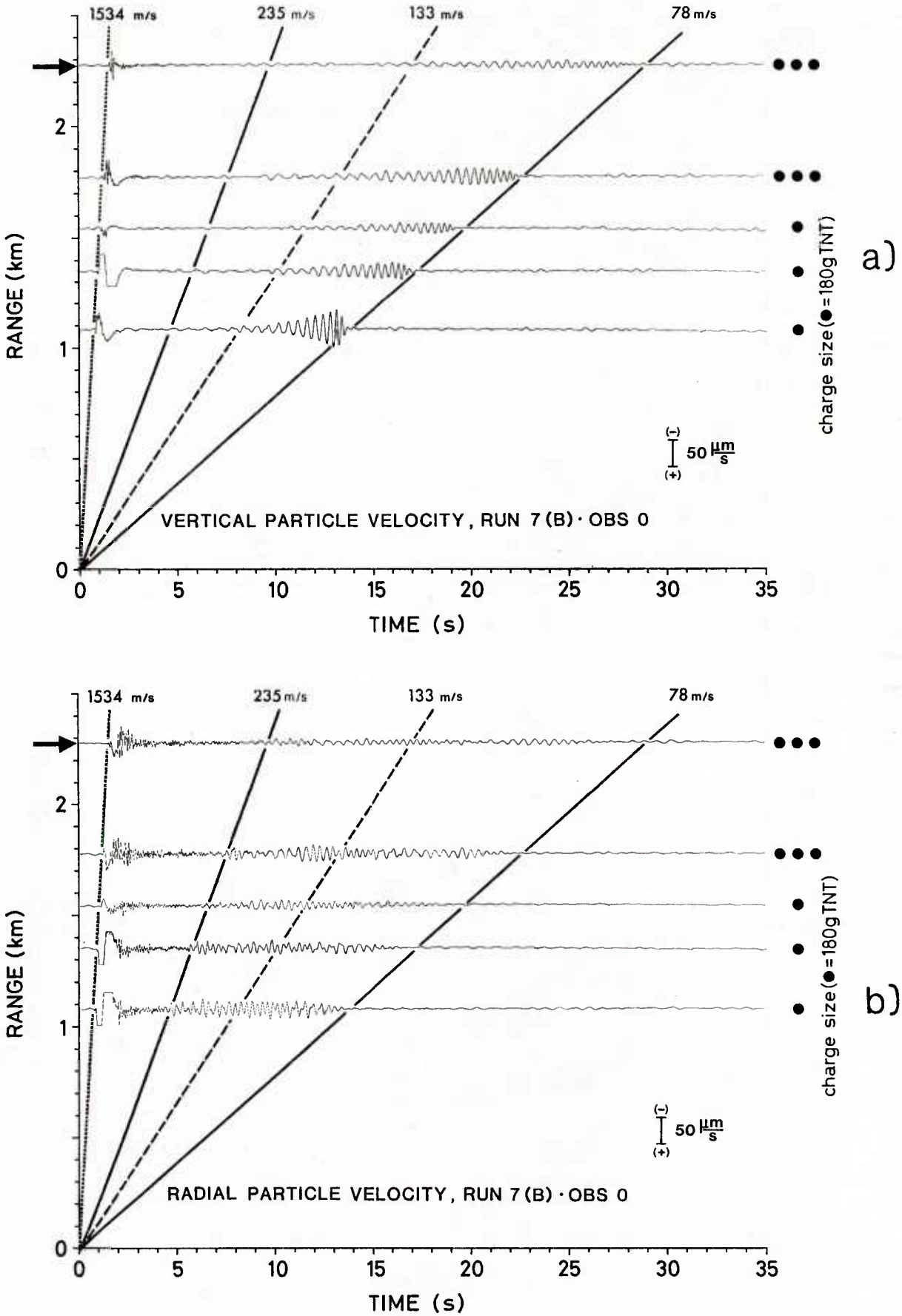

FIG. 22 SITE G, RUN 7(B): TIME/DISTANCE PLOTS (distant OBS)
a. Vertical component
b. Radial component

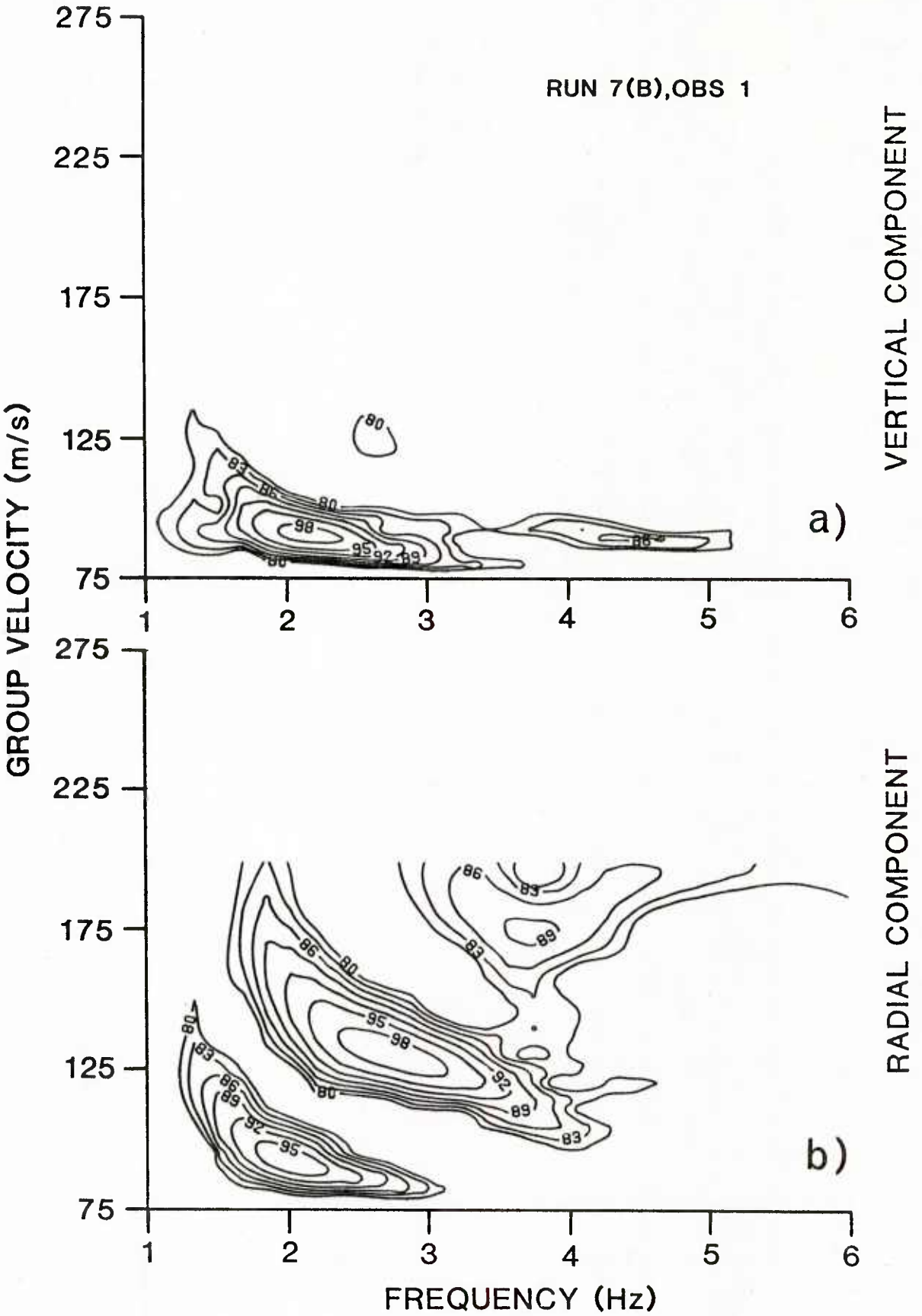

FIG. 23 SITE G, RUN 7(B): AMPLITUDE CONTOURS FROM EVENT "→" OF FIG. 21 (close OBS)
a. Vertical component
b. Radial component

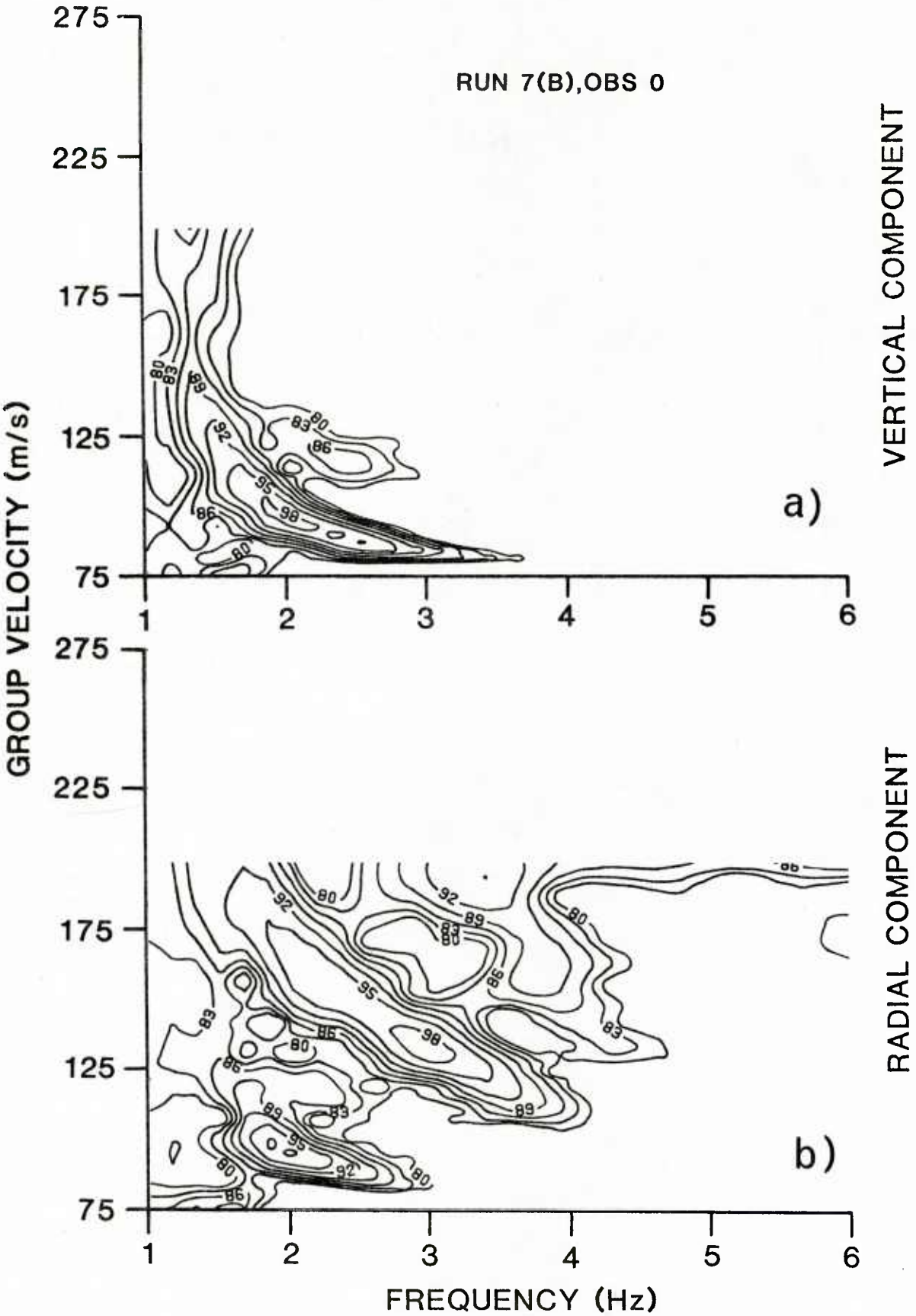

FIG. 24 SITE G, RUN 7(B): AMPLITUDE CONTOURS FROM EVENT "→" OF FIG. 22 (distant OBS)
a. Vertical component
b. Radial component

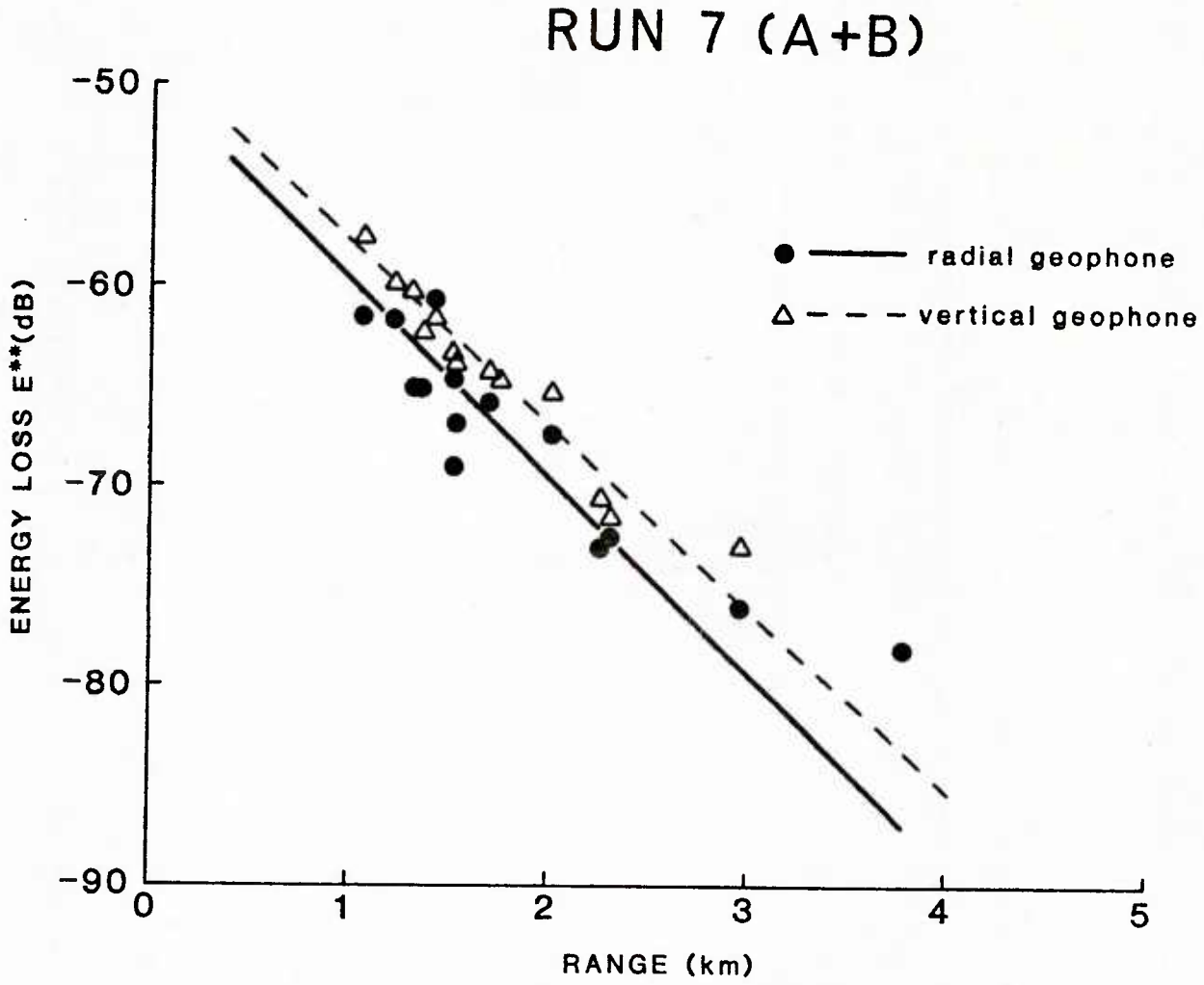

FIG. 25 SITE G, RUN 8: ATTENUATION CURVES FROM RUN 7 (A & B)

4.4 Experiment R

4.4.1 General

Table 5 summarizes conditions at site R (Fig. 1), where two runs were performed.

TABLE 5

CONDITIONS AT SITE R

ID	Date	Position Long/Lat	Runs	Bottom Type	Water depth	OBS deployed
R	May 81	Off Viareggio 10°04.2'E 43°48.6'N	# 8 # 9	Layered sediments, higher consolidation	30 m	3 at <60 m distance

The three OBS units were deployed in a triangle, with spacings of less than 60 m. Such a compact deployment offers a good opportunity to estimate and cross-check the fidelity of each sensor by comparing corresponding seismograms and obtaining information on the spatial coherence of the signals recorded.

The explosive charges were fired along two paths, one to the southeast (run 8) and one to the south (run 9), as illustrated by the dashed sectors in Fig. 1.

During this experiment the shot instant was also transmitted via radio to synchronize the data acquisition on the computer. Thus the alignment of the seismograms in the time/distance domain was easier and more accurate.

4.4.2 Run 8

Figures 26a and 27a show the time/distance plots (from two of the OBS units) from run 8, as sensed by the vertical geophones. The front of the interface wavetrain is characterized by 1.5 to 2 Hz oscillations with 250 m/s velocity, the tail by low-velocity (65 m/s) 2.5 to 3 Hz oscillations.

A particular wavelet with consistent frequency/velocity characteristics is again clearly visible in the centre of the wavetrain. It is marked on the figures by a dashed line that corresponds to a velocity of 145 m/s with a frequency of about 4 Hz. This particular wavelet is much more pronounced in the radial particle velocity component represented in the time/distance

plots of the corresponding Figs. 26b and 27b (and also in Fig. 28, obtained from the third OBS unit).

A comparison of the seismograms obtained from different OBS units — for example Fig. 26a with Fig. 27a (vertical sensor) or Fig. 26b with Fig. 27b (radial sensor) — reveals a high degree of similarity and congruency, even up to fine details. This demonstrates again the good quality of the data. However, the similarity of the data from different OBS stations is valid only for the interface wave train, the effects of the water wave being reproduced with different phases and intensities. This depends obviously on the actual physical orientation of the OBS with respect to the incoming shock wave.

A dispersion analysis of an event in run 8 is displayed in Fig. 29. The amplitude contours of both the vertical and the radial component immediately reveal the origin of the pronounced wavelet mentioned above: the first, higher mode reveals hardly any dispersion, whereas the fundamental mode is highly dispersed, as indicated by the steepness of the dispersion curve at frequencies below 2.8 Hz. This suggests a quite abrupt change in the layering, with a high shear-velocity gradient in that frequency (wavelength) range.

As expected from the vicinity of this site to site P (about 5 miles), the amplitude contours from the two sites are very similar (compare Fig. 29 with Fig. 8) and with regard to the fundamental mode (or up to 2.5 to 3 Hz) there is a conclusive and satisfactory agreement. The dispersive curve of the first mode at this site R, however, is shifted towards lower group velocities by about 40 m/s. A qualitative explanation for this shift at frequencies above 3 Hz is based on the deeper penetration of the low-frequency contributions at this site: the larger wavelengths are thus influenced by the same sub-bottom, whereas the energy flow of the higher frequencies is restricted to the obviously different top layers. This distinction between the two sites concerning the first mode is also confirmed by the associated contour plots of the phase between the radial and vertical component (not shown here): at this site (R) there is a retrograde particle motion in the first mode, while at site P there is a prograde particle motion. As expected from the consistency of the amplitude contours at these sites, the hodographs of the fundamental mode are prograde in both cases. The results at site R are comparable to those recently published by Essen et al <23>.

Analyzing the time/distance plots together with the amplitude contours shows that the first mode is clearly distinguished by horizontally aligned hodographs and the fundamental mode by vertically aligned hodographs with low eccentricity. It should be mentioned that the amplitude contours of Fig. 29b also indicates the second mode, which has 3 to 5 Hz oscillations, group-velocities around 250 m/s and, as the associated phase contours show, retrograde polarization.

Preceding the water-wave (1520 m/s) on all time/distance plots (Figs. 26 to 28) are two (thin) solid lines: V_1 = 1715 m/s and V_2 = 2850 m/s, belonging to the direct p-wave (compressional wave) and a refracted p-wave, respectively. The 1715 m/s line starts at the origin, while the 2850 m/s line is

time-shifted by about 0.7s,[1] the so-called "intercept-time", T_i. From the classical literature on geophysical prospecting <25>, the depth Z_1 of the refracting layer can be calculated as:

$$T_i = 2Z_1 \frac{\sqrt{(V_2^2 - V_1^2)}}{V_1 V_2} .$$

The formula is valid under the assumption of parallel layering and constant sound speed, V_1, in the first sediment layer (no sound-speed gradient). Assuming this, Z_1 has been calculated to be about 750 m.

Figure 30 presents attenuation curves based on the data of run 8. These demonstrate low attenuation of the vertical and radial component, with the values:

vertical component: $\alpha_V \approx 3$ dB/km,
radial component: $\alpha_r \approx 4$ dB/km.

4.4.3 Run 9

The time/distance plots and contour plots of run 9 presented in Figs. 31 to 33 essentially confirm the results of run 8. The individual seismograms are slightly different from those of run 8 due to a stronger LF-noise background. The peculiar wavelet in the middle of the interface wavetrain in Figs. 31 and 32 seems to propagate somewhat faster (153 m/s), as is also indicated by the contour plots of Fig. 33.

Comparing the seismograms recorded by different OBS units, Fig. 31b with Fig. 32, for instance, again demonstrates the outstanding congruence of the measured data, at least of the interface-wave contributions.

The attenuation curves of Fig. 34 are based on the run-9 data and give the following attenuation coefficients:

vertical component: $\alpha_V \approx 2$ dB/km,
radial component: $\alpha_r \approx 3$ dB/km.

These are comparable to those from run 8.

[1] Extracted from the large-scale original time/distance plots.

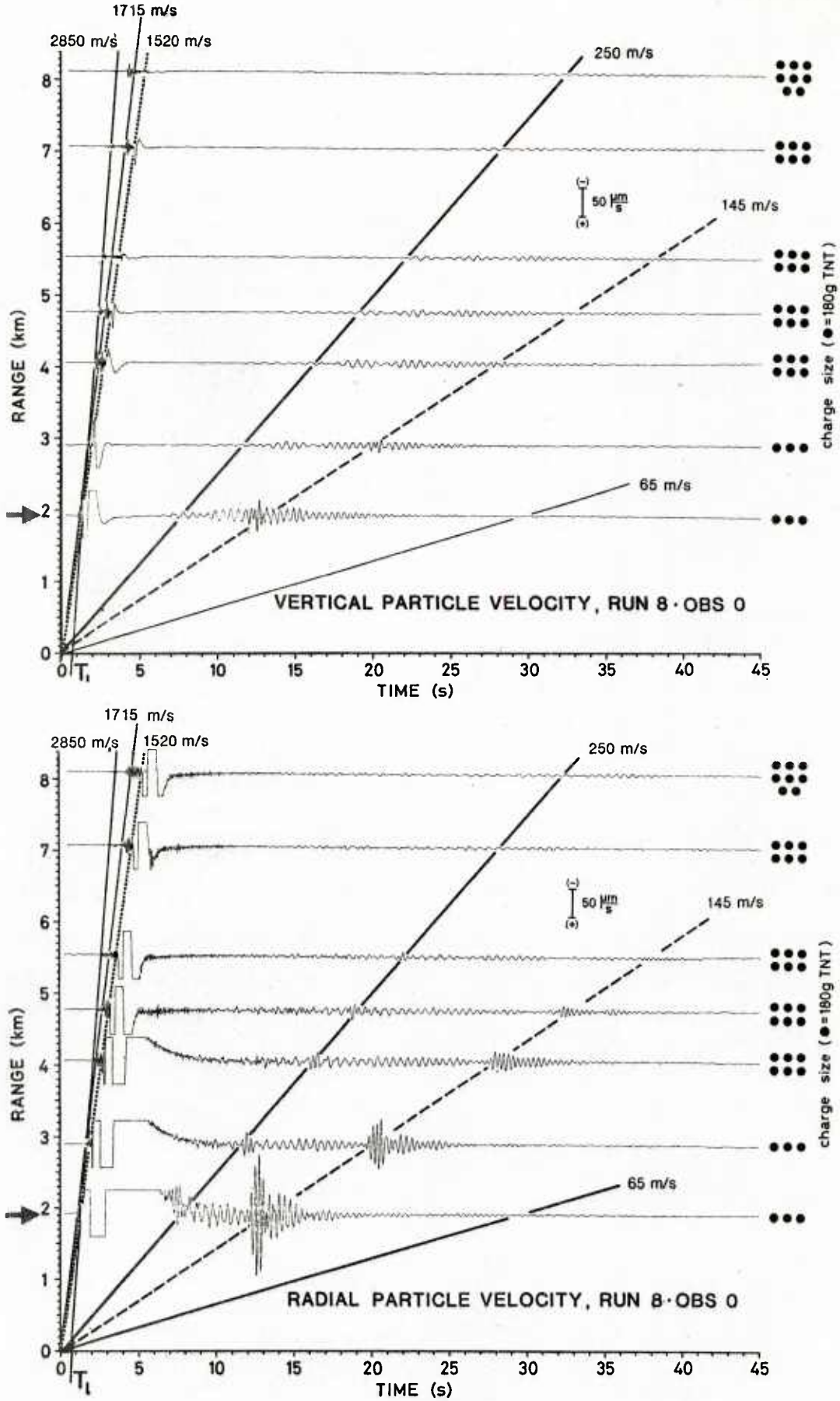

FIG. 26 SITE R, RUN 8: TIME/DISTANCE PLOTS (first OBS)
a. Vertical component
b. Radial component

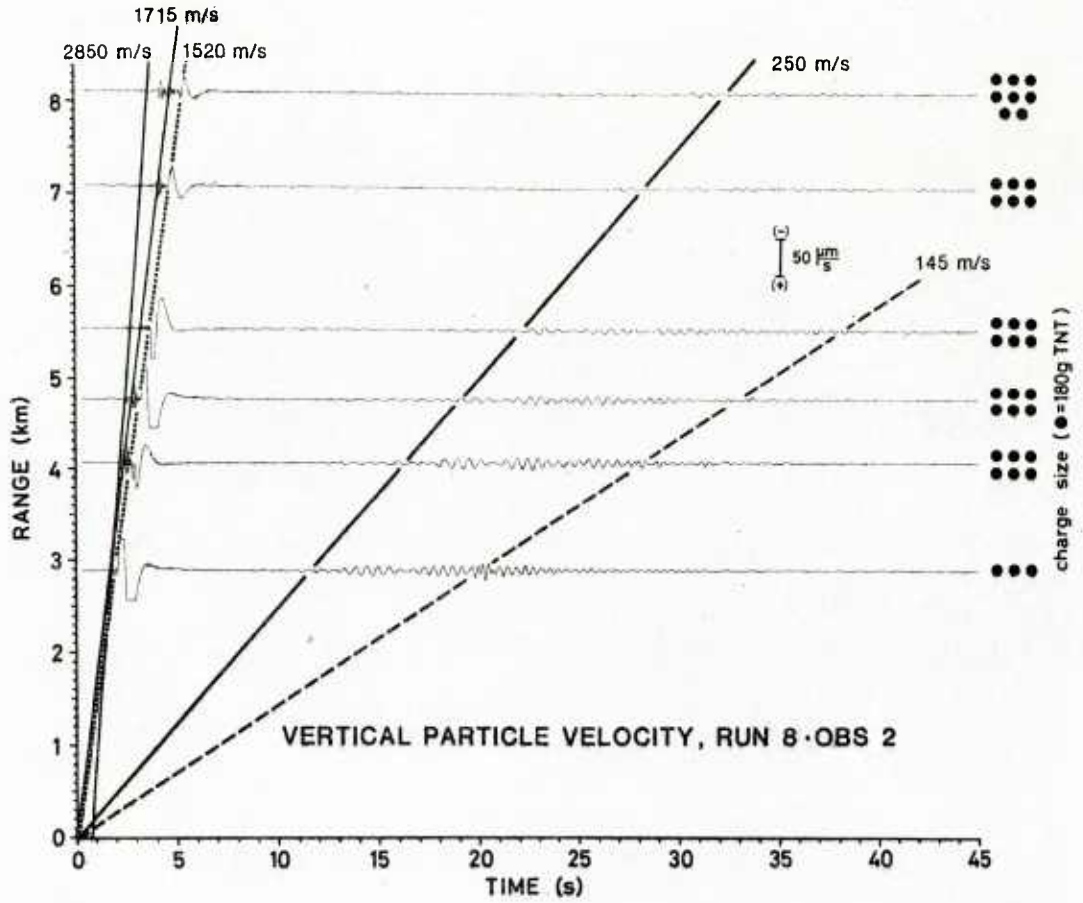

a)

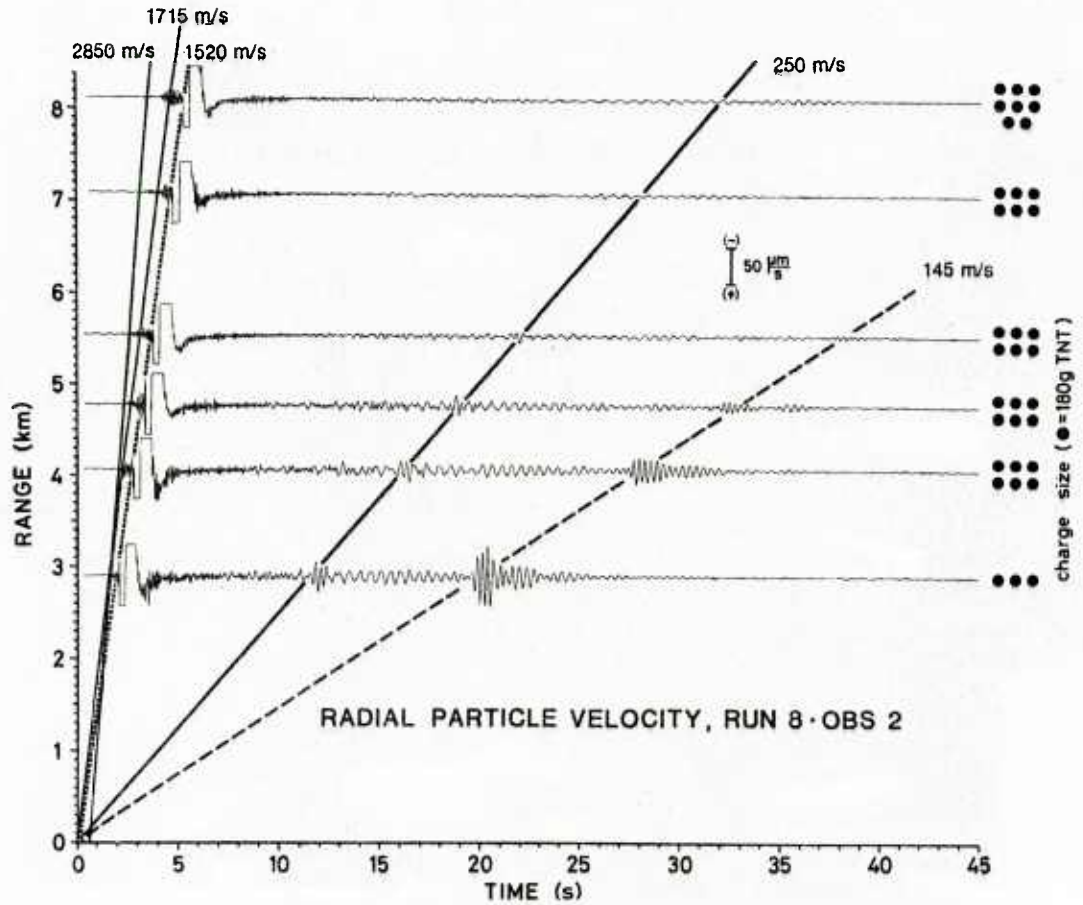

b)

FIG. 27 SITE R, RUN 8: TIME/DISTANCE PLOTS (second OBS)
a. Vertical component
b. Radial component

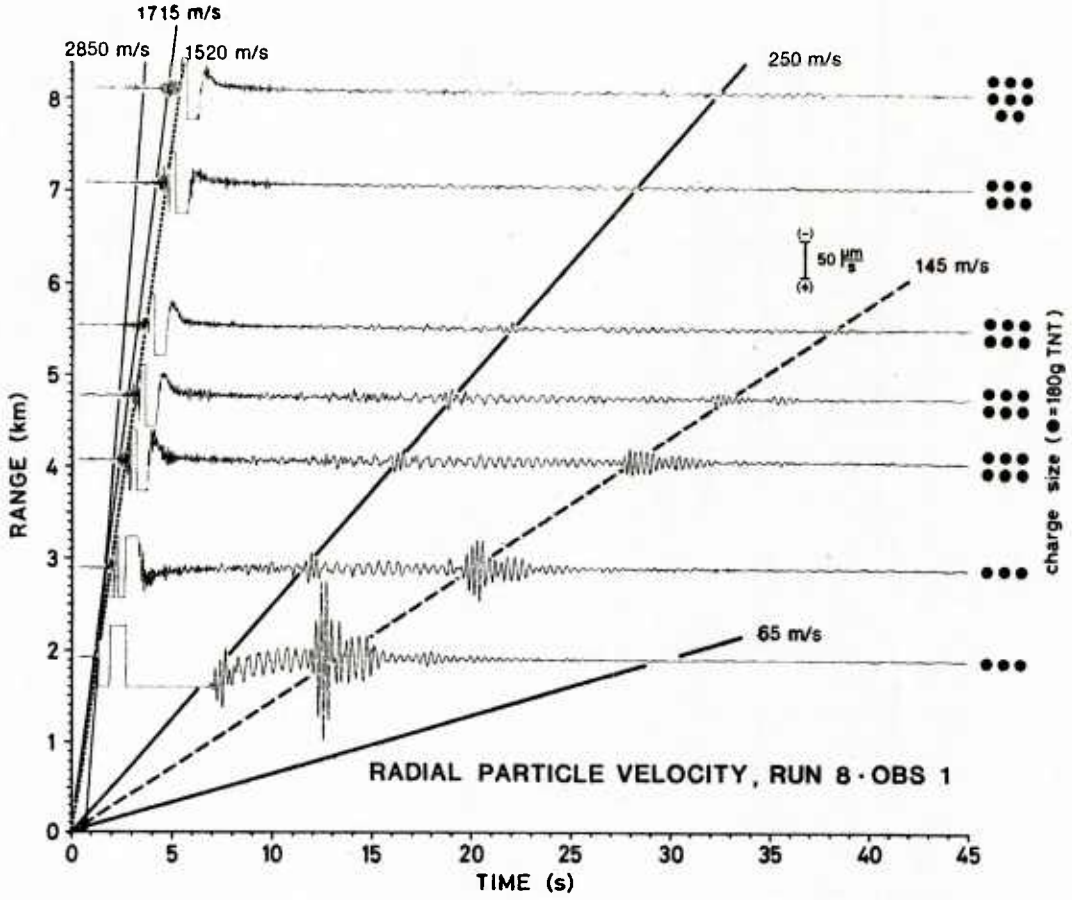

FIG. 28 SITE R, RUN 8: TIME/DISTANCE PLOTS (third OBS) Radial component only

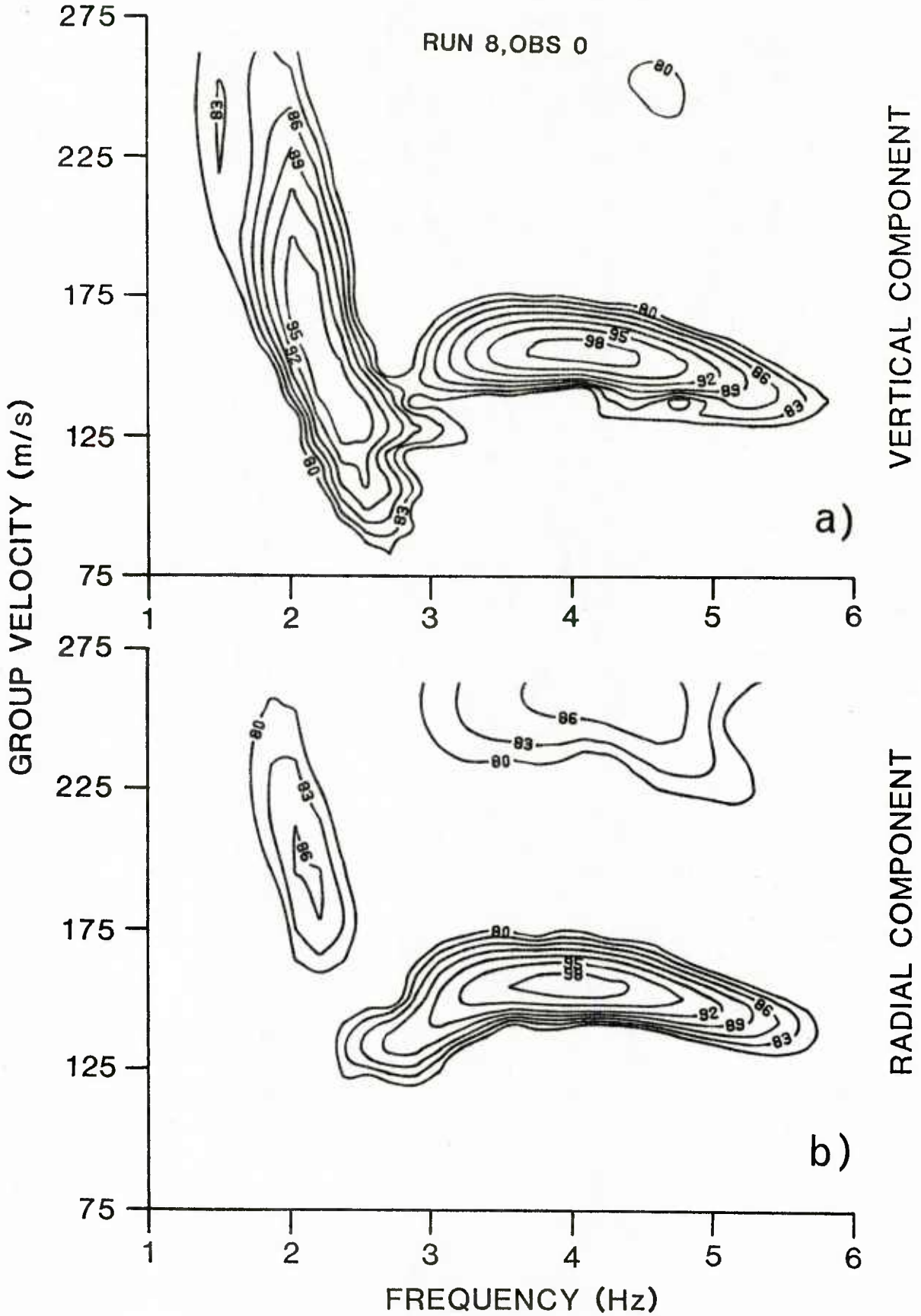

FIG. 29 SITE R, RUN 8: AMPLITUDE CONTOURS FROM EVENT "→" OF FIG. 26 (first OBS)

a. Vertical component

b. Radial component

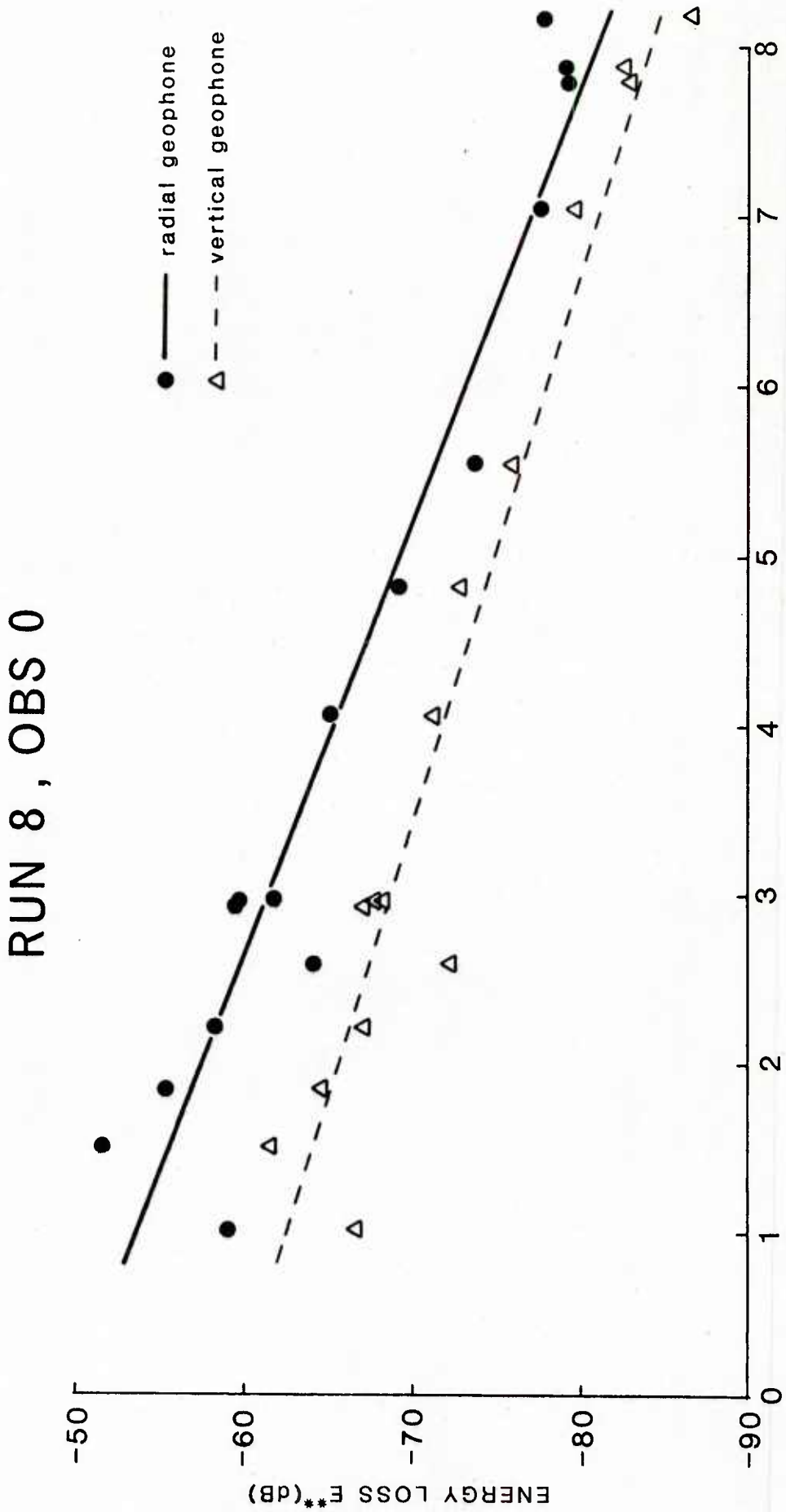

FIG. 30 SITE R, RUN 8: ATTENUATION CURVES

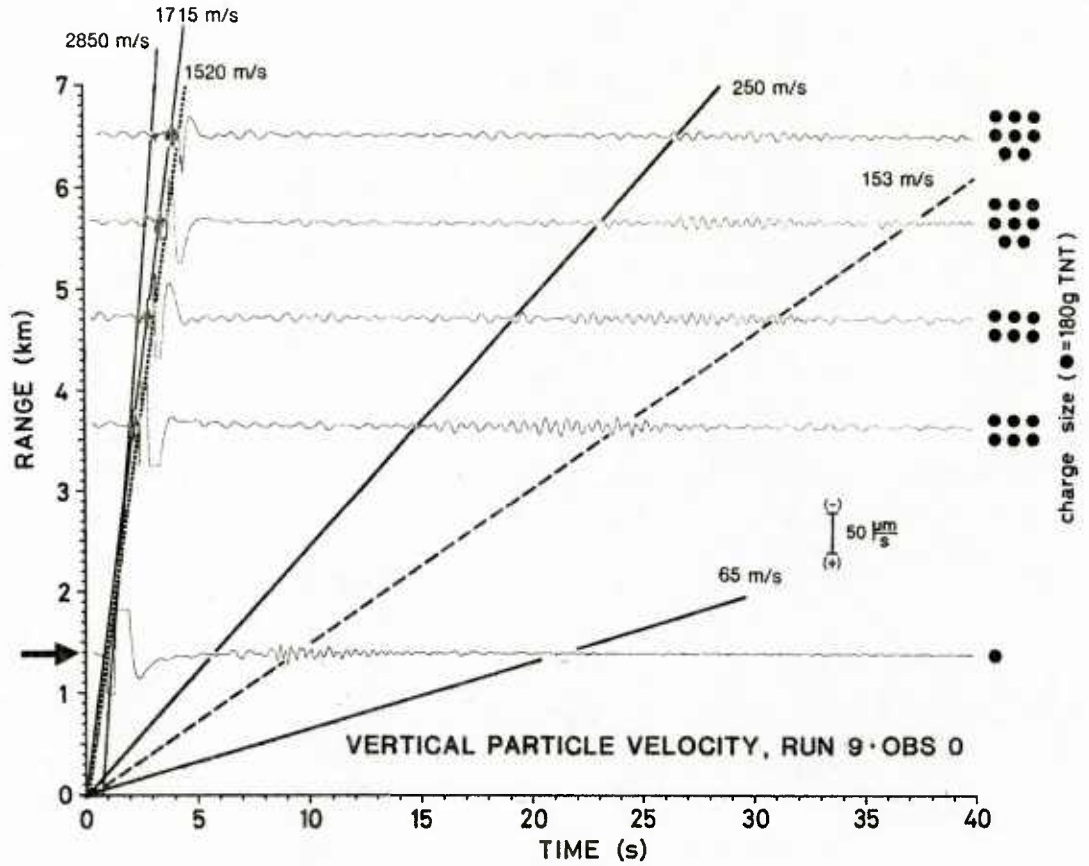

a)

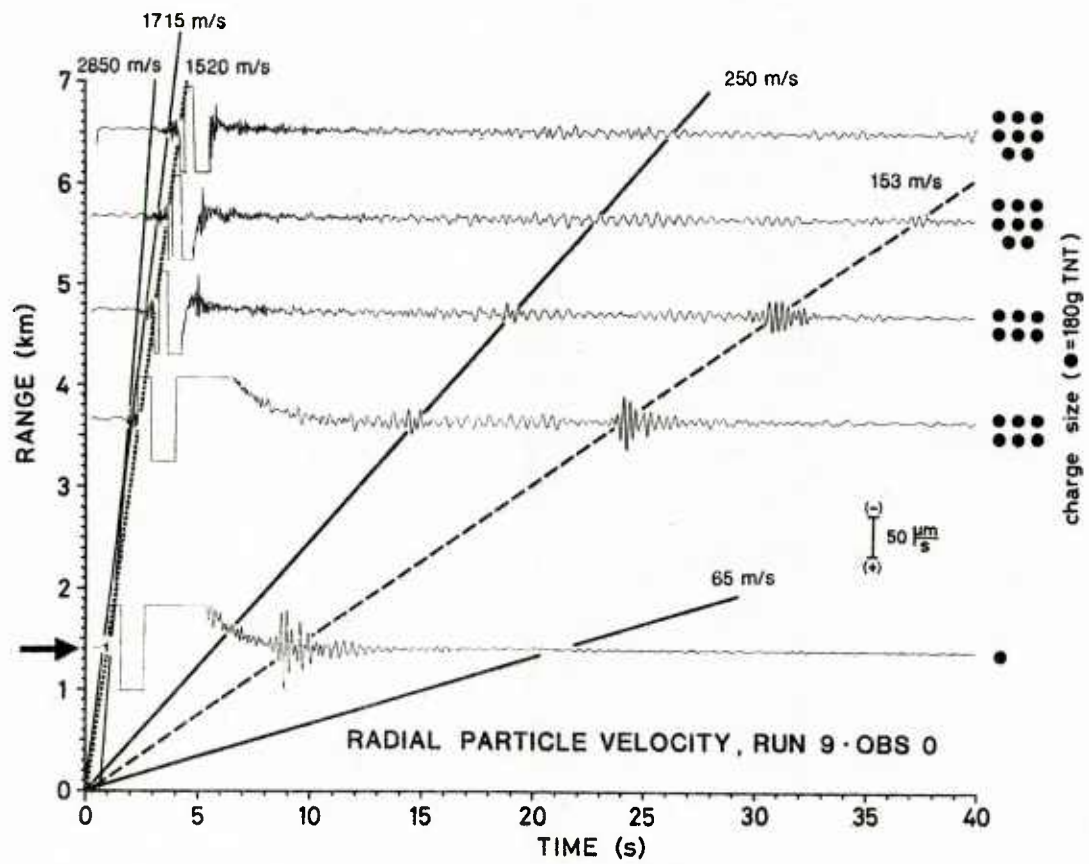

b)

FIG. 31 SITE R, RUN 9: TIME/DISTANCE PLOTS (first OBS)
a. Vertical component
b. Radial component

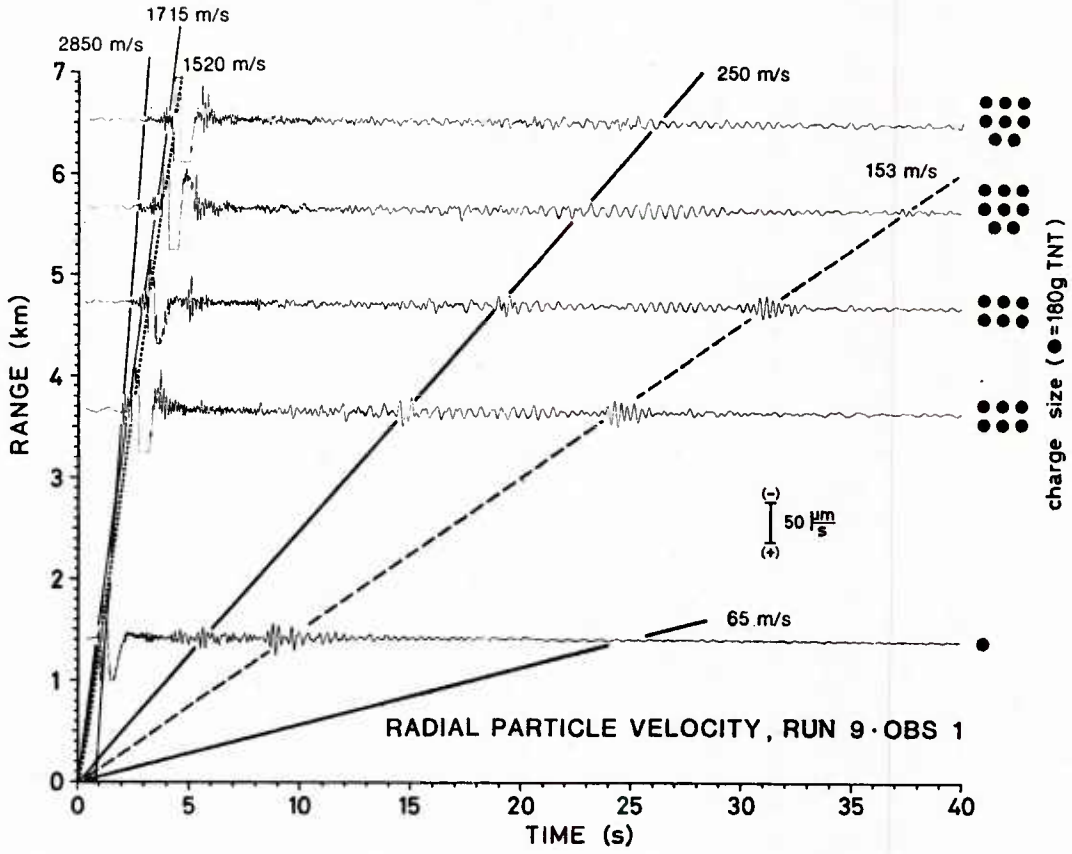

FIG. 32 SITE R, RUN 9: TIME/DISTANCE PLOTS (second OBS) Radial component only

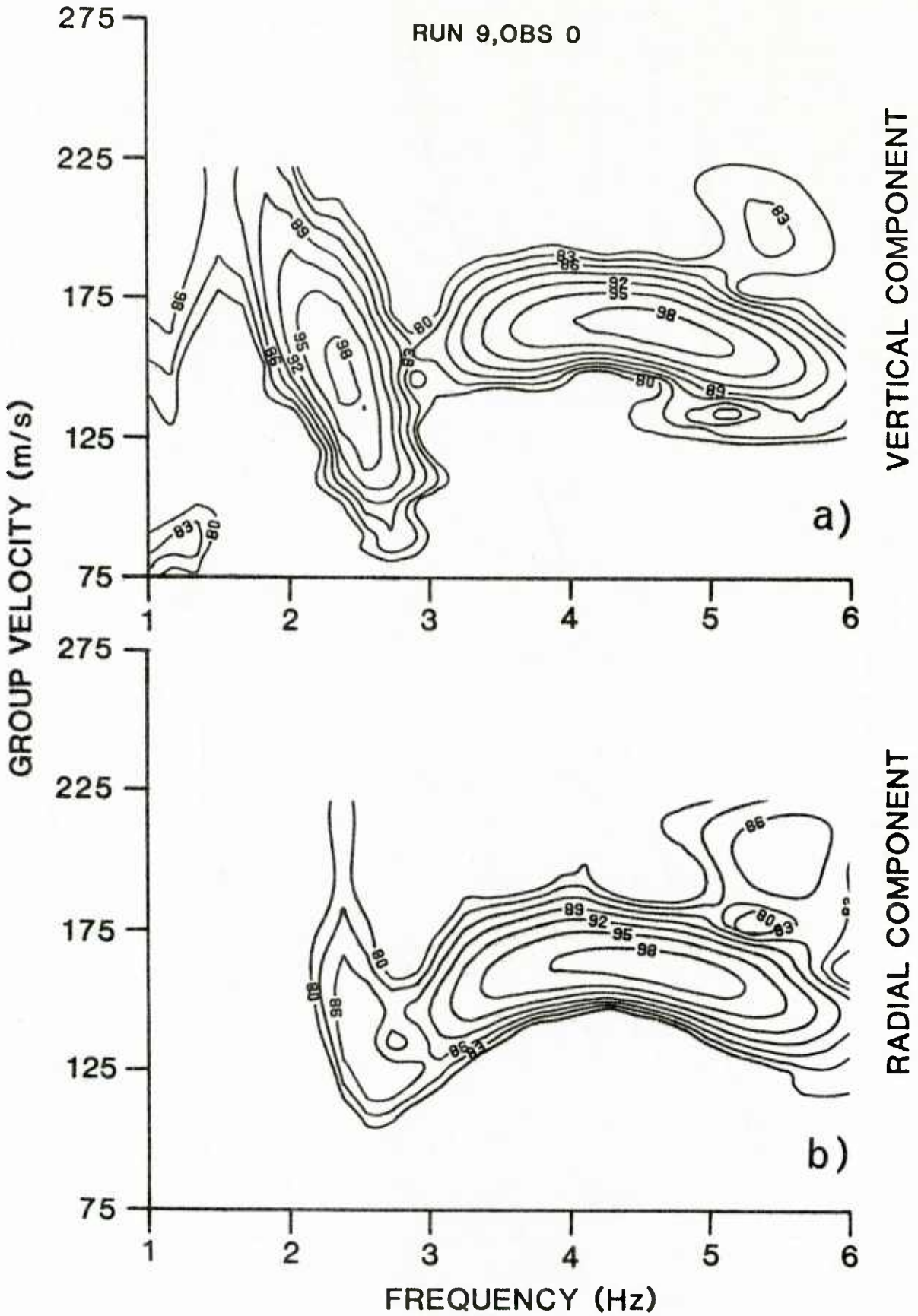

FIG. 33 SITE R, RUN 9: AMPLITUDE CONTOURS FROM EVENT "→" OF FIG. 31 (first OBS)
a. Vertical component
b. Radial component

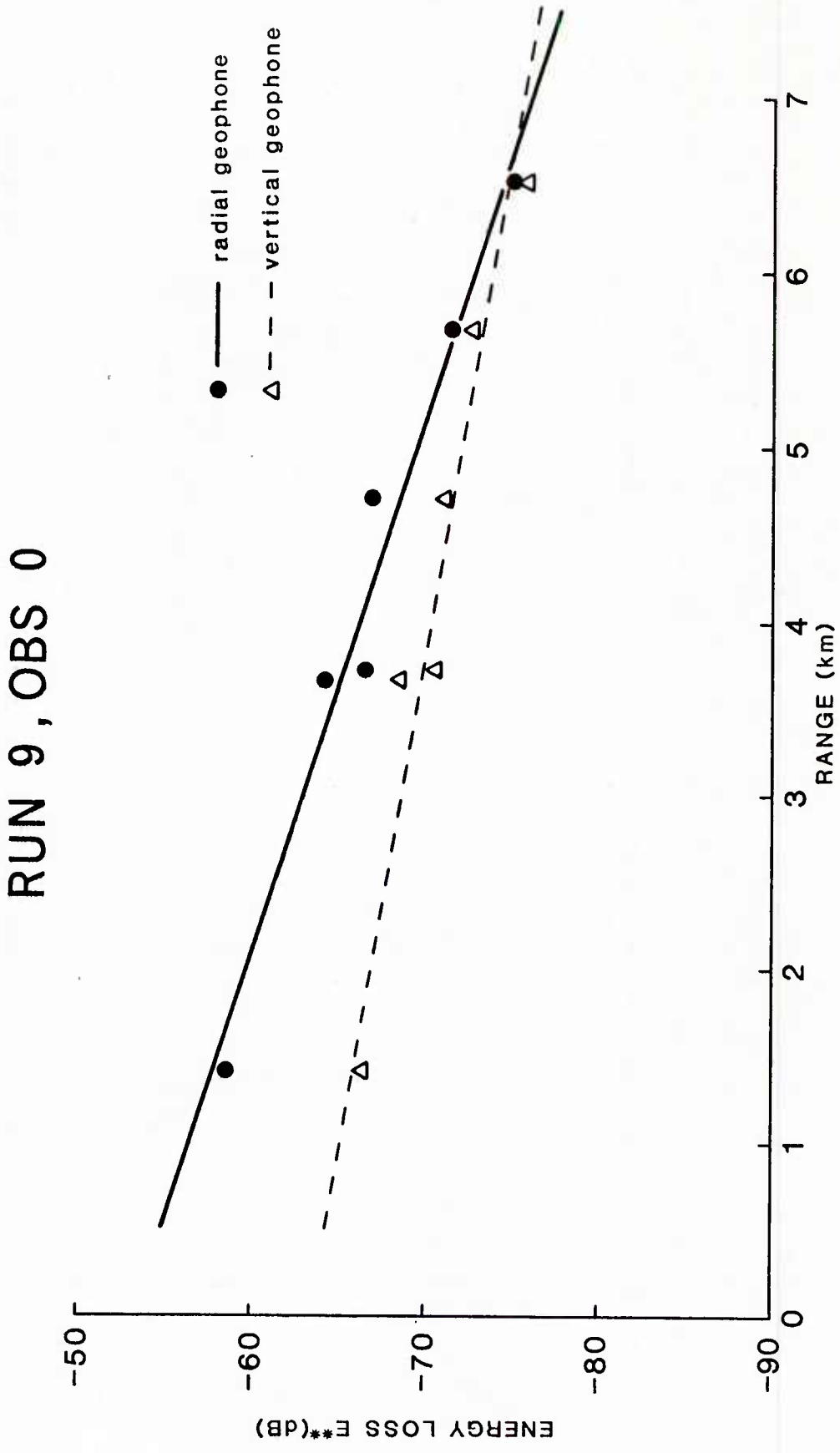

FIG. 34 SITE R, RUN 9: ATTENUATION CURVES

CONCLUSIONS

The results obtained from time/distance plots, dispersion analysis, and attenuation curves are summarized as follows:

1. At all locations the existence of the interface wave could be demonstrated. It exhibited characteristic low-frequency, slow wavetrains, usually split into different, dispersive modes.

2. The frequencies in the wavetrains ranged from 1.5 to 5.5 Hz on the soft bottoms and from 2.5 to 7.5 Hz on the harder bottom; medium values in the fundamental mode are about 2.5 Hz and about 5 Hz, respectively.

3. The associated speeds were from 50 to 300 m/s; the main contributions (fundamental mode) were around 125 m/s for the soft bottom and around 225 for the hard bottom.

4. The seismograms usually showed normal dispersion ("lower frequencies propagate faster"). Slightly anomalous dispersion was observed only on the hard bottom.

5. Up to three propagation modes could be demonstrated, clearly distinguished by different propagation speeds and particle motions in the radial/vertical plane (hodographs). These were:

   On soft bottoms:

   - A fundamental mode, always with prograde motion and vertically aligned.
   - A first mode, with either prograde or retrograde motion and horizontally aligned.
   - A second mode, always retrograde motion and horizontally aligned.

   On the hard bottom:

   - A fundamental mode, with retrograde motion and vertically aligned.
   - A first mode, with prograde motion and vertically aligned.

6. The calculated attenuation coefficients (averaged over the entire wavetrain) ranged from 2 to 10 dB/km for the vertical particle velocity and 3 to 10 dB/km for the radial one. These results are in good agreement with similar data from the North Sea <23>.

7. A qualitative attempt was made to explain some particular features of the dispersion curves by the shear parameters of the underlying sediment structure.

It is concluded that interface waves can be used to compute the shear properties of the sea-floor. To achieve this requires comprehensive modelling and geophysical investigations together with further measurements of interface waves.

ACKNOWLEDGEMENTS

SACLANTCEN wishes to thank Dr. H.-H. Essen of the Institute of Geophysics of the University of Hamburg for making available his program of the multiple-filter technique.

The following SACLANTCEN personnel also contributed to this work:

Electronic Eng. Dept	M. Michelozzi	Sea trials
Environmental Acoustics Group	G. Guidi	Data analysis
Environmental Modelling Group	M. Ferla	Contour-plotting routine

REFERENCES

1. ROEVER, W.L., VINING, T.F. and STRICK, E. Propagation of elastic wave motion from an impulsive source along a fluid/solid interface. Philosophical Transaction of the Royal Society, 251A, 1959: 465-523.

2. CAGNIARD. L. Reflection and Refraction of Progressive Seismic Waves. New York, N.Y., McGraw-Hill, 1962.

3. RAUCH, D. Seismic interface waves in coastal waters: a review, SACLANTCEN SR-42. La Spezia, Italy, SACLANT ASW Research Centre, 1980.

4. BRADNER, H. Pressure variations accompanying a plane wave propagated along the ocean bottom. Journal of Geophysical Research, 67, 1962: 3631-3633.

5. BRADNER, H. Probing sea-bottom sediments with microseismic noise. Journal of Geophysical Research, 68, 1963: 1788-1791.

6. LATHAM, G.V. and SUTTON, G.H. Seismic measurements on the ocean-floor. I. Bermuda area. Journal of Geophysical Research, 71, 1966: 2545-2573.

7. HAWKER, K.E. Influence of Stoneley waves on plane-wave reflection coefficients: Identification of the Stoneley wave mechanism, TP-77-45. Austin, TX, University of Texas, Applied Research Laboratory. 1977.

8. HAWKER, K.E. Influence of Stoneley waves on plane-wave reflection coefficients: Characteristics of bottom reflection loss. Journal of the Acoustical Society of America, 64, 1978: 548-555.

9. RAUCH, D. Experimental and theoretical studies of seismic interface waves in coastal waters. In: KUPERMAN, W.A. and JENSEN, F.B., eds. Bottom-Interacting Ocean Acoustics. Proceedings of a conference held at SACLANTCEN on 9-13 June 1980. and New York, NY, Plenum, 1980: pp. 307-327. (NATO Conference Series IV, Marine Sciences 5).

10. RAUCH, D. and SCHMALFELDT, B. Ocean-bottom interface waves of the Stoneley/Scholte-type: properties, observations and possible use. In: Pace, N.G. ed. Acoustics and the Sea-Bed, Proceedings of an Institute of Acoustics, Underwater Acoustics Group Conference. Bath, UK, Bath University Press, 1983: 307-316.

11. SCHMALFELDT, B. and RAUCH, D. Ambient and ship-induced noise in shallow water. In: KUPERMAN, W.A. and JENSEN, F.B., eds. Bottom-Interacting Ocean Acoustics. New York, NY, Plenum, 1980: pp. 329-343. Proceedings of a conference held at SACLANTCEN (NATO Conference Series IV, on 9-13 June 1980. Marine Sciences 5).

12. JENSEN, F.B. and KUPERMAN, W.A. The optimum frequency of propagation in shallow water environments. Journal of the Acoustical Society of America, 73, 1983: 813-819.

13. BARBAGELATA, A., MICHELOZZI, E., RAUCH, D., and SCHMALFELDT, B. Seismic sensing of extremely-low-frequency sounds in coastal waters. In: Institute of Electrical and Electronics Engineers, Acoustics Speech and Signal Processing Society. Proceedings, IEEE International Conference on Acoustics, Speech and Signal Processing, (ICASSP 82) Paris, France, 3-5 May 1982. Piscataway N.J., IEEE Service Center, 1982: pp. 1878-1881.

14. BLACKINGTON, J.G. and ODEGARD, M.E. An ocean-bottom seismograph using digital telemetry and floating-point conversion. IEEE Transactions on Geoscience Electronics, 15, 1977: 74-82.

15. DZIEWONSKI, A., BLOCH, S. and LANDISMAN, M. A technique for the analysis of transient seismic signals. Bulletin of the Siesmological Society of America, 59, 1969: 427-444.

16. DZIEWONSKI, A. and HALES, A.L. Numerical analysis of dispersed seismic waves. In: Methods in Computational Physics, Vol. 11, Seismology: Surface Waves and Earth Oscillations. New York, N.Y., Academic Press, 1972: pp. 39-85.

17. SEIDL, D. and MÜLLER, S. Seismische Oberflächenwellen. Journal of Geophysics, 42, 1977: 283-328.

18. ESSEN, H.H. Model computations for low-velocity surface waves on marine sediments. In: KUPERMAN, W.A. and JENSEN, F.B., eds. Bottom-Interacting Ocean Acoustics. Proceedings of a conference held at SACLANTCEN on 9-13 June 1980. New York, NY, Plenum, 1980: pp. 299-305.

19. SCHMIDT, H. Excitation and propagation of interface waves in a stratified sea-bed. In: Pace, N.G. ed. Acoustics and the Sea-Bed, Proceedings of an Institute of Acoustics, Underwater Acoustics Group Conference. Bath, UK, Bath University Press, 1983: pp. 327-334.

20. BRADNER, H. and DODDS, J.G. Comparative seismic noise on the ocean bottom and on land. Journal of Geophysical Research, 69, 1964: 4339-4348.

21. BRADNER, H., DODDS, J.G. and FOULKS, R.E. Investigation of microseism sources with ocean-bottom seismometers. Geophysics, 30, 1965: 511-526.

22. BRADNER, H. and LATHAM, G.V. Prograde Rayleigh waves and microseism sources. Journal of Geophysical Research, Vol. 77, 1972: 6422-6426.

23. ESSEN, H.-H., JANLE, H., SCHIRMER, F. and SIEBERT, J. Propagation of surface waves in marine sediments. Journal of Geophysics, 49, 1981: 115-122.

24. BROCHER, T.M., IWATAKE, B.T., GETTRUST, J.F., SUTTON, G.H. and FRAZER, L.N. Comparison of the S/N ratios of low-frequency hydrophones and geophones as a function of ocean depth. Bulletin of the Seismological Society of America, 71, 5, 1981: 1649-1659.

25. DOBRIN, M.B. Introduction to Geophysical Prospecting. New York, N.Y., McGraw-Hill, 1976: p. 296.

APPENDICES

APPENDIX A

ACQUISITION AND PRE-PROCESSING OF SEISMIC DATA

On board the receiving ship the VHF signals from the radio buoys were received, demodulated and recorded both on magnetic tape and on computer disc.

The digital data streams from all three OBS units were stored simultaneously on the same magnetic tape by writing two different traces for each OBS unit, one trace being used as backup. Two of the remaining traces were always assigned to the time base and the on-line comments (clock and voice).

In parallel with the magnetic-tape recording, the data coming from each OBS via an interface were decoded and passed to one or two HP-21MX computers with disc units and to different displays and plotters. Thus all events could be recorded simultaneously on disc and immediately pre-processed without interfering with the on-going experiment.

The pre-processing software ("GEOS" system developed by SACLANTCEN) has three options:

a. The plot of the time series

   This option simultaneously displays all four channels of each OBS unit, either before or after digital filtering. It also transforms the coordinates of the horizontal geophone's reference axes.

b. The vector display

   This option plots any two components on a screen: in other words the visual presentation of particle hodographs.

c. Fast evaluation on board

   For a fast evaluation of the data during the experiment a standard version of this 4-channel plot was made for each OBS unit. This graphic display of the original data permits identification of the arrival times and gives an idea about the magnitudes and frequencies of the different wavetypes involved. The true propagation direction was determined by applying the vector display option to the water arrival or the interface wavetrain. Thereafter, the 4-channel plots were repeated with an adequate filtering and a proper coordinate rotation of the reference axis (into the radial and transverse components). Thus an optimal graphic display of the interesting phenomena was obtained. The high-quality (lineprinter) plots can be used without further treatment to assemble the time/distance plots presented in the main text (see the example in Fig. 6a).

APPENDIX B

DISPERSION ANALYSIS WITH THE "MULTIPLE-FILTER TECHNIQUE"

The multiple-filter technique has proved to be a very powerful tool for analyzing multimode dispersed signals. As this technique is well documented in the literature <B.1, B.2, B.3> and the mathematical background is given in <B.4> the description will be limited to general features. Some of the most significant parameters of the program version are given later in parenthesis to facilitate future data comparisons or tests.

The SPADA-formatted data are fed into the SACLANTCEN UNIVAC computer (via its mini-filing system) where they are decimated and compensated for the mean value. To ensure a sufficient high-frequency resolution of the signal spectra (512 frequency samples, Δf = 0.043 Hz), relatively long signal-windows (20.48 s, corresponding to 1024 time samples) have to be fourier-transformed. Short signal-windows may be expanded by adding an appropriate number of zeros; however, this artificial filling was unnecessary in this case, since sufficient ambient noise was usually recorded at the end of the interface wavetrain.

The seismogram section is then fourier analyzed, $s(t) \rightarrow s(f)$, yielding a spectrum up to the maximum frequency of 25 Hz. (For this and the following derivations refer also to Fig. B.1, which is based on the paper of Dziewonski et al <B.1>).

The frequency range of interest (usually 1 to 6 Hz) is subdivided into a suitable number N (N = 30) of frequency samples, f_n, which define the N columns of the so-called Gabor matrix. The maximum and minimum of the pertinent range of group-velocities v_m is given automatically by the starting point and the end point of the chosen time window.

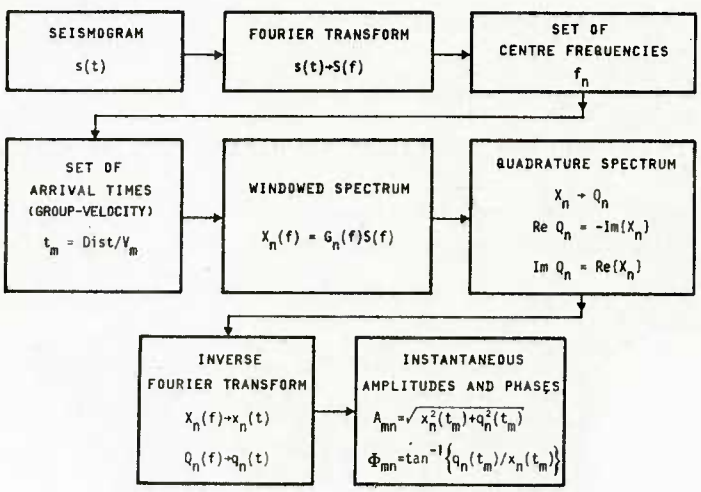

Fig. B.1

The resulting group-velocity interval (typically 50 to 250 m/s) is also subdivided by an adequately high number M (such as M = 45) of velocity samples v_m (or equivalent arrival time t_m = distance/v_m). These latter sampling points define the M rows of the Gabor matrix, which form the underlying grid for the final sampling of the amplitude or phase results. Gaussian weighting-functions, $G_n(f)$, are defined around all these centre frequencies, f_n, with an appropriate decay representing a set of optimal narrow-band filters with constant gain and required resolution:

$$G_n(f) = \exp\left\{-\beta \frac{(f - f_n)^2}{f_n}\right\} \text{for } (1-B)f_n < f < (1+B)f_n \quad \text{(Eq. B.1)}$$

$$G_n(f) = 0 \quad \text{elsewhere}$$

(β = 100 and B = 0.2 have proved to be suitable values for our studies). In the following, this set of N = 30 bandpass windows, G_n, is applied to the seismogram (strictly speaking to its fourier transform) at all the M = 45 pre-selected travel times, t_m, (or group-velocities, v_m); or in other words the seimogram is "scanned" in the velocity/frequency domain.

The inverse fourier transformation of these windowed spectra, $G_n(f)S(f)$, would yield a set of narrow-band filtered components, $s_n(t)$, in which the original time series s(t) has been decomposed. Interest, however, lies not only in the detailed reconstruction of these so-called in-phase components but in the general trends of these band-limited signals with regard to amplitude and phase-shift. Thus it is necessary to extract the slowly varying envelopes, $A_n(t)$, and phase shifts, $\phi_n(t)+\theta_n$, (or phase modulation) from these components, which can be represented in the form:

$$s_n(t) = A_n(t) \exp\{2\pi i f_n(t) + \phi_n(t) + \theta_n\}. \quad \text{(Eq. B.2)}$$

These low-frequency am/fm modulations of the pre-selected "carriers" may be obtained in a very simple way from the already existing in-phase spectra, $X_n(f)$:

$$X_n(f) = G_n(f)S(f) = \text{Re}\{X_n(f)\} + i\,\text{Im}\{X_n(f)\} \quad \text{(Eq. B.3)}$$

by also forming the so-called quadrature spectra $Q_n(f)$:

$$Q_n(f) = -\text{Im}\{X_n(f)\} + i\{\text{Re } X_n(f)\}, \quad \text{(Eq. B.4)}$$

where Re and Im refer to the real and imaginary parts, respectively.

Inverse fourier transformation of these spectra, $X_n(f)$ and $Q_n(f)$, gives two time functions $x_n(t)$ and $q_n(t)$, which permits the following representation of the signals:

$$s_n(t) = [x_n(t) + iq_n(t)] \exp\{2\pi i\, f_n(t)\}. \quad \text{(Eq. B.5)}$$

Comparing Eq. B.5 with Eq. B.2 it is realized that the interesting terms $A_n(t)$ and $\phi_n(t) + \theta_n$ may be calculated immediately from the quadrature functions according to

$$\phi_{mn}(t_m)=\arctan\{q_n(t_m)/x_n(t_m)\};\ A_{mn}(t_m) = \sqrt{\{x_n^2(t_m) + q_n^2(t_m)\}}. \quad \text{(Eq B.6)}$$

The resulting M elements, A_{mn} and ϕ_{mn}, of the n-th column of the pertinent Gabor matrix sample the envelope and phase-shift of the n-th spectral component with respect to all pre-selected group velocities v_m (or arrival time t_m). Accordingly, the N elements of the m-th row of these matrices sample the pertinent contributions for a given v_m (or t_m) with respect to all spectral components. Usually, the amplitude matrices, $\{A_{mn}\}$ are plotted numerically or contoured [normalized and scaled according to 20 log $(A_{mn}/A_{max})_\nu$] for each given sensor (ν = x,y,z) or post-aligned coordinate direction (ν = or r,t,z). In contrast to this, the final phase-matrix outputs are mainly comparisons between two sensors or orthogonal directions μ and ν:

$$\{\Delta\phi_{mn}\}_{\mu\nu} = \{\phi_{mn}\}_\mu - \{\phi_{mn}\}_\nu$$

revealing the existence and stability of certain phase relations between the most significant motion components. In the present report, however, only the amplitude contour plots, A_{mn}, are presented.

The version of the "multiple-filter program" used was made available to SACLANTCEN by Dr. H.H. Essen of the Institute of Geophysics of the University of Hamburg (Germany) <B.5>.

REFERENCES

B.1 DZIEWONSKI, A., BLOCH, S. and LANDISMAN, M. A technique for the analysis of transient seismic signals. Bulletin of the Seismological Society of America, 59, 1969: 427-444.

B.2 DZIEWONSKI, A. and HALES, A.L. Numerical analysis of dispersed seismic waves. In: Methods in Computational Physics, Vol. 11, Seismology: Surface Waves and Earth Oscillations. New York, N.Y., Academic Press, 1972: pp. 39-85.

B.3 SEIDL, D. and MÜLLER, S. Seismische Oberflächenwellen. Journal of Geophysics, 42, 1977: 283-328.

B.4 GRACE, O.D. and PITTS, S.P. Signal processing by digital quadrature techniques, DRL-TR-68-39. Austin , TX, University of Texas, Defence Research Laboratory, 1968.

B.5 ESSEN, H.-H., JANLE, H., SCHIRMER, F. and SIEBERT, J. Propagation of surface waves in marine sediments. Journal of Geophysica, 49, 1981: 115-122.

APPENDIX C

ATTENUATION ANALYSIS BY MEANS OF THE "SPECA" SYSTEM

For a versatile off-line data analysis on small computers a special software package, named "SPECA", has been designed to calculate simultaneously the power-, coherence- and phase-spectra for up to eight channels or two OBS units.

However, the work reported in the main text used mainly the option for power-spectrum estimation and an option to integrate those spectra within selectable frequency ranges. This tool is adequate for deriving the attenuation curves of the interface waves when the spectral analysis is restricted to that part of the seismogram that contains the interface wave train and when the integration extends to the relevant frequency range only (i.e. about 1.5 to 5.5 Hz).

As usual, the initial step for all further processing is the proper alignment of the horizontal coordinate system to achieve the common radial and transverse components (radial means — as usual — parallel to source-receiver direction).

As the interface wavetrain always forms the tail of the seismogram, the same analysis window may be applied to all records. A window length of 13.7 s (corresponding to 8192 samples) was chosen, which turned out to be sufficient since it included the whole interface wave contributions (and some ambient noise). This 13.7 s section was then divided into three 50% overlapping, Hann-weighted sub-series. Finally, the power spectral density was obtained by summing the corresponding three power spectra of the sub-series (f_{max} = 300 Hz, Δf = 0.146 Hz).

In order to obtain the energy involved in the interface wavetrains these power spectra must then be integrated, as mentioned above. The resulting energy values, 10 log E(dB), were then corrected for the actual charge size and geometrical spreading. With one TNT block of m_0 = 180 g as reference quantity, the effect of the actual charge size m(g) was then corrected for each event according to the formula <C.1>:

$$10 \log E^* = 10 \log E + 13.3 \log (m/m_0) \quad .$$

By choosing the minimum source/receiver distance of r_0 = 560 m as a second reference quantity, the energy decay due to the cylindrical shape of the relevant wave fronts could be corrected for by the relation:

$$10 \log E^{**} = 10 \log E^* + 10 \log (r/r_0) \quad .$$

The graphs used in the main text (see Fig. 6c, for example) plot these twice-corrected energy values, 10 log E**, against the distance r. Assuming a residual decay law of the form:

$$E^{**} \sim \exp(-\alpha r) \text{ (i.e. } 10 \log E^{**} \sim \alpha r),$$

this logarithmic representation of the data points may be approximated by a straight line (regression analysis)[1] which is shown in the above-mentioned graphs. The slopes of these fitted lines correspond to the plane-wave attenuation factor α, which is a measure of the loss due to absorption and scattering.

REFERENCES

C.1 URICK, R.J. Principles of Underwater Sound, 2nd edn. New York, N.Y., McGraw-Hill, 1975: p. 89.

C.2 KERTZ, W. Statistik geophysikalischer Beobachtungsreihen (Manuscript Brochure). Braunschweig, Institut für Geophysik und Meteorologie der Technischen Universität, 1970.

---

[1] If both coordinates x_n and y_n of a group of N points have similar margins of error, the optimal regression line is calculated according to the formula <C.2>

$$y - \overline{y} = \alpha(x - \overline{x}) \quad ,$$

with

$$\overline{x} = 1/N \, \Sigma \, x_n, \quad \overline{y} = 1/N \, \Sigma \, y_n \, .$$

The slope α is calculated by the formula:

$$\alpha_{1,2} = - 1 \pm \sqrt{\{1/A^2 + 1\}} \quad ,$$

with

$$A = \frac{2 \, L_{xy}}{L_{xx} - L_{yy}} \quad \text{and} \quad L_{xy} = N(\Sigma x_n y_n) - (\Sigma x_n)(\Sigma x_n) \quad \text{and} \quad L_{xx} = N(\Sigma x_n x_n) - (\Sigma x_n)(\Sigma x_n).$$

One of the resulting slopes $\alpha_{1,2}$ characterizes the wanted line with minimized distances to all points while the other slope belongs to the orthogonal line with maximized distances.

INITIAL DISTRIBUTION

	Copies
MINISTRIES OF DEFENCE	
MOD Belgium	2
DND Canada	10
CHOD Denmark	8
MOD France	8
MOD Germany	15
MOD Greece	
MOD Italy	
MOD Netherlands	
CHOD Norway	
MOD Portugal	2
MOD Turkey	
MOD U.K.	16
SECDEF U.S.	
NATO AUTHORITIES	
Defence Planning Committee	
NAMILCOM	
SACLANT	
SACLANTREPEUR	
CINCWESTLANT/COMOCEANLANT	
COMSTRIKFLTANT	1
COMIBERLANT	1
CINCEASTLANT	1
COMSUBACLANT	1
COMMAIREASTLANT	1
SACEUR	2
CINCNORTH	1
CINCSOUTH	1
COMNAVSOUTH	1
COMSTRIKFORSOUTH	1
COMEDCENT	1
COMMARAIRMED	1
CINCHAN	1

	Copies
SCNR FOR SACLANTCEN	
SCNR Belgium	1
SCNR Canada	1
SCNR Denmark	1
SCNR Germany	1
SCNR Greece	1
SCNR Italy	1
SCNR Netherlands	1
SCNR Norway	1
SCNR Portugal	1
SCNR	1
SCNR	1
SCNR	2
SECDEF SCNR	1
NAMILCOM Rep. SCNR	1
NATIONAL LIAISON OFFICERS	
NLO Canada	1
NLO Denmark	1
NLO Germany	1
NLO	1
NLO U.K.	1
NLO U.S.	1
NLR TO SACLANT	
NLR Belgium	1
NLR Canada	1
NLR Denmark	1
NLR Germany	1
NLR Greece	1
NLR Italy	1
NLR Netherlands	1
NLR Norway	1
NLR Portugal	1
NLR Turkey	1
NLR UK	1
NLR US	1
Total initial distribution	238
SACLANTCEN Library	10
Stock	32
Total number of copies	280